Raman spectroscopy of graphite intercalation compounds: charge transfer, strain, and electron-phonon coupling in graphene layers

Julio C. Chacón-Torres[1 *], Ludger Wirtz[2] and Thomas Pichler[3]

[1] Freie Universität Berlin, FB Physik, Institut für Experimental Physik, Arnimallee 14, 14195 Berlin, Germany
[2] Physics and Materials Science Research Unit, University of Luxembourg, Campus Limpertsberg, L-1511 Luxembourg, Luxembourg
[3] Faculty of Physics, University of Vienna, Strudlhofgasse 4, A-1090 Vienna, Austria

Received XXXX, revised XXXX, accepted XXXX
Published online XXXX

Key words: Graphite Intercalation Compounds, Graphene, Strain, Charge Transfer, and Electron Phonon Coupling.

[*] Corresponding author: e-mail julio.chacon@fu-berlin.de, Phone:+49-30-838-56152, Fax:+49-30-838-56081

Graphite intercalation compounds (GICs) are an interesting and highly studied field since 1970's. It has gained renewed interest since the discovery of superconductivity at high temperature for CaC_6 and the rise of graphene. Intercalation is a technique used to introduce atoms or molecules into the structure of a host material. Intercalation of alkali metals in graphite has shown to be a controllable procedure recently used as a scalable technique for bulk production of graphene, and nano-ribbons by induced exfoliation of graphite. It also creates supramolecular interactions between the host and the intercalant, inducing changes in the electronic, mechanical, and physical properties of the host. GICs are the mother system of intercalation also employed in fullerenes, carbon nanotubes, graphene, and carbon-composites. We will show how a combination of Raman and ab-initio calculations of the density and the electronic band structure in GICs can serve as a tool to elucidate the electronic structure, electron phonon coupling (EPC), charge transfer, and lattice parameters of GICs and the graphene layers within. This knowledge of GICs is of high importance to understand superconductivity and to set the basis for applications with GICs, graphene and other nano-carbon based materials like nanocomposites in batteries and nanoelectronic devices.

1 Introduction Graphite is a mineral with a rich chemistry mainly based in its amphoteric character, i.e. being, both, an electron donor or acceptor material. This results from its electronic structure having an electron affinity as well as ionization potential of around 4.6 eV [1]. In order to tailor the electronic properties of graphite, several groups [2–6] used the technique of so called "intercalation" to introduce additional chemical species in between the layers of graphite as a way to modulate the electronic transport and optical properties.

This was also analyzed in detail regarding the effects of effective charge transfer, and structural changes such as lattice expansion, stacking order and internal strain. More recently this was used for an improved graphene production by exfoliation [8].

GICs are formed by consecutive stacking of graphene layers and intercalant layers. Common intercalants are alkali-metals (K, Li, Cs, Rb), alkali-earth-metals (Be, Ca, Ba), rare-earth elements or molecular groups such as $FeCl_3$, AsF_5, H_2SO_4, HNO_3, etc. All the above form different tri-dimensional macro-molecules, each one with intrinsic electronic, physical and chemical properties [2, 3, 9–15]. The properties that distinguish every GIC directly depend on the specific chemical species which occupy the carbon interlayer space. The intercalants are consequently classified as donors or acceptors according to

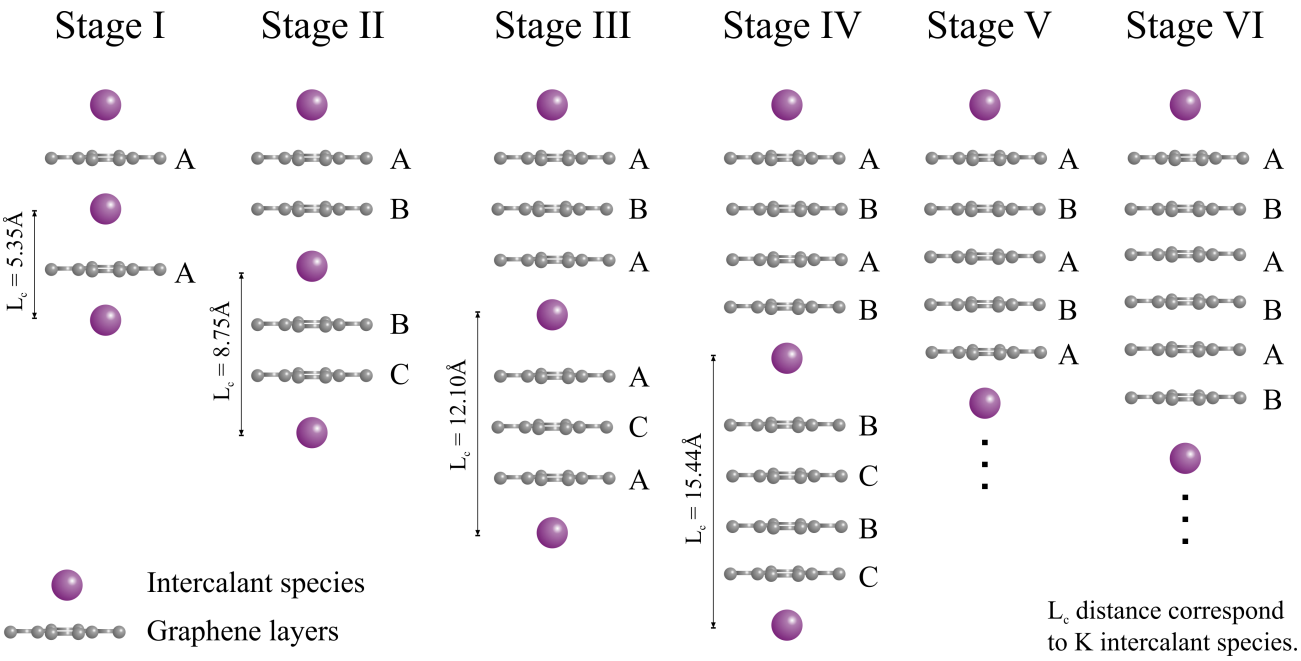

Figure 1 Schematic diagram illustrating the staging in graphite intercalation compounds for stages I to VI adapted from [7]. Intercalant layers are indicated as purple balls, and the graphene layers by gray honeycomb networks. The distances L_c represent the interplanar distance when potassium acts as intercalant.

whether they donate or extract electrons from the graphitic layers. Examples of electron-donor GICs are KC_8, CaC_6, LiC_6, whereas molecules such as $FeCl_3$, and AsF_5 act as electron-acceptors [2]. In both cases, donor/acceptor GICs, the stoichiometric concentration of intercalants with respect to carbon atoms can be varied creating highly ordered macro-molecular structures with different number of graphene layers in between intercalant ones (see Fig. 1). This effect has been called "staging" [2] defining the number of graphene layers in between adjacent planes of intercalant by an index n.

As depicted in Fig. 1 each GIC has a number of intercalant and graphite layers defining its stage and a unique stacking order defining the orientation of the individual graphene layers in c-axis direction. For stage I, each graphene layer is followed by an intercalant one (AA stacking order). Stage II, means two subsequent graphene layers (AB-stacked) surrounded by intercalant ones. Stage III consists of three graphene layers in ABC-stacking in between intercalants. For all higher staged GICs shown in the left side of the figure the presence of ABA-stacking, as well as BCB- and ACA- stacking following a sequence described by Eq. 1 and Eq. 2 [16]:

$$\left|(AB)_{n/2}|(BC)_{n/2}|(CA)_{n/2}\right| \quad for\ even\ \boldsymbol{n}, \tag{1}$$

$$\left|A(BA)_{(n-1)/2}|A(CA)_{(n-1)/2}\right| \quad for\ odd\ \boldsymbol{n}. \tag{2}$$

The content of intercalant in each stage is determined from the stoichiometric formula XC_{12_n} with the exception of the stage I compound whose chemical formula is XC_8 or XC_6, where X is the type of intercalant. Thus, we have for instance KC_8, LiC_6, CaC_6 as stage I, KC_{24} as stage II and KC_{36} as stage III, etc. in different GICs. This article will mainly focus on these alkali and alkaline earth GICs.

2 Structure and Stage Identification in GICs

As the properties in GICs are strongly dependent on the concentration of intercalants, an accurate stage index determination is crucial. The stage determination in GICs has been mainly performed by X-ray diffraction (XRD) using $(00l)$ reflections [17](see Fig. 2). From the diffraction angles θ_l corresponding to every $(00l)$ reflection in XRD one can calculate the c-lattice constant (distance between intercalant layers, L_c) by applying Bragg's law:

$$l\lambda = 2L_c \sin\theta_l. \tag{3}$$

The stage index n is then given by the relation [18–20]

$$L_c = nc_0 + d_i = (n-1)c_0 + d_s. \tag{4}$$

In the latter formula c_0 is the distance between adjacent graphite layers ($c_0 = 3.35$ Å) and $d_s = c_0 + d_i$ is the distance between two graphite layers with an intercalant layer in between. In Table 1 a compilation (from Ref. [9]) of different XRD studies as function of the stage is shown, revealing that d_s and c_0 are essentially independent of stage.

The structure and arrangement of atoms in GICs are governed by the *Nearest Layer* (NL) model early defined by Nemanich and Solin [21, 22]. The kinetics of the transformation between stages in GICs follows the Daumas-Hérold model [23]. This model predicts a transitional dynamics of intercalation between stages

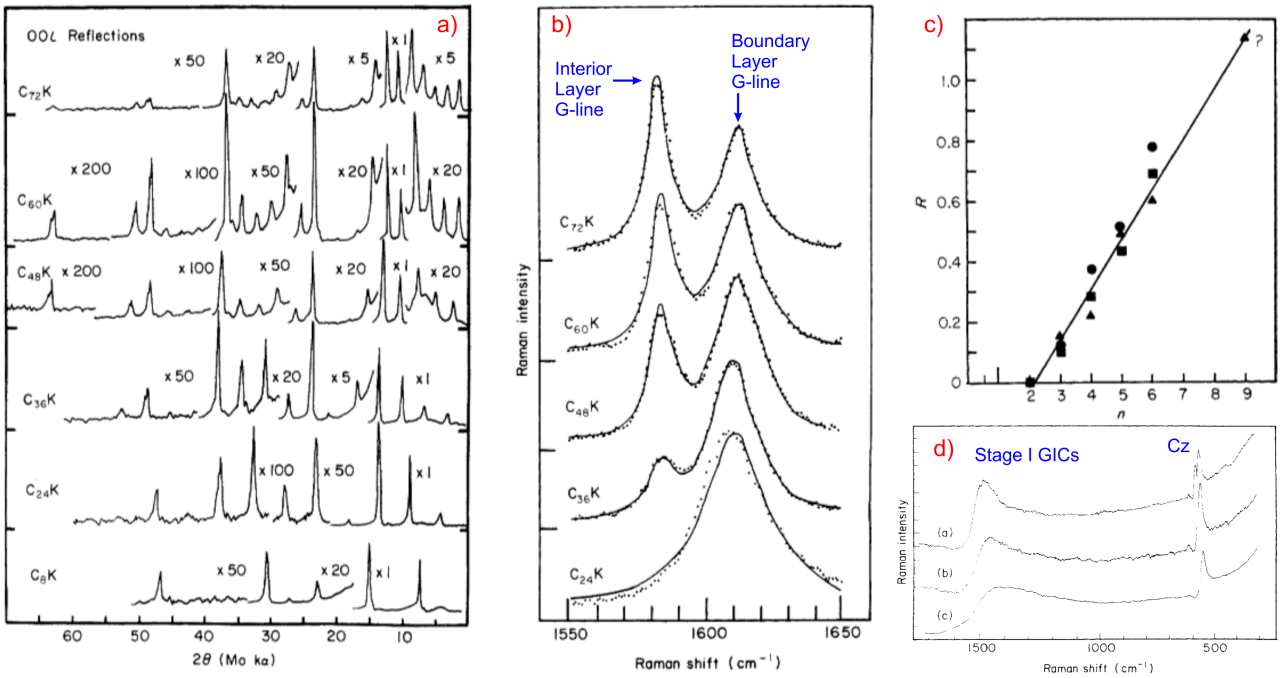

Figure 2 Figure adapted from Ref. [17]. a) XRD diffraction patterns from potassium GICs ranging from stage I to VI. b) Archetypal Raman spectrum for K doped graphite ($2 \leq n \geq 6$) intercalation compounds at 514 nm, frequently used as a bench mark for stage identification. c) Intensity ratio ($R = I_{uc}/I_c$) for $n \geq 2$ K, Rb, and Cs samples. d) Raman response of Stage I alkali metal GICs: (a) CsC_8, (b) RbC_8, and (c) KC_8 depicting a broad Fano line-shape with an intense and characteristic C_z mode. Reproduced by permission of John Wiley and Sons Publishing.

Table 1 C-lattice constant L_c for graphite-potassium intercalation compounds from Ref. [9]

L_c (experimental) $\AA$, Stage ($n =$)	I	II	III	IV
Rüdorff and Schulze	5.41	8.77	12.12	15.49
Nixon and Parry	5.35	8.72	12.10	15.45
Underhill	5.32	8.74	12.07	15.44
Calculated $(5.41 + 3.35(n-1)\AA)$	5.41	8.76	12.11	15.46

in which the existence of completely unfilled layers is not possible but partially filled layers may coexist in the same system. Therefore, the staging is governed by the configurations observed in Fig. 1. The first configuration shows the possibility to have single graphene layers surrounded by intercalant layers. The second configuration consists of two carbon layers with intercalant boundary regions. Finally, the third system presents the possibility to have a mixture of graphene layers surrounded by intercalant layers plus a single graphene layer in between. An extension of this model is observed at the right side of Fig. 1 where the number of single graphene layers adjacent to other graphene layers increases as increasing the stage n.

In order to fully support the previous assumptions within the NL model, a combination of Raman spectroscopy with XRD in GICs [17, 25] was performed to assign and analyze the vibrational response with respect to the individual stage. GICs with Stages I to VI with Cs, Ca, and K were studied (see Fig. 2 b-d). For stages higher than III Solin and Nemanich observed in K-GICs the presence of two G-line components, one close to pristine graphite and one blue-shifted [26], which change in intensity as function of stage. On the other hand, for stage II a single nearly symmetric Lorentzian line around 1600 cm^{-1} and for stage I a clear strongly broadened and red shifted Fano line-shape independent from the intercalant and a characteristic z-axis C_z mode are observed. (see Fig. 2 b-d). The *Nearest Layer* model was invoked to explain the splitting and intensity of the G-line components for $n \geq 3$ (see Fig. 2 b). A relative intensity ratio R can be extracted from the two G-line components intensity and plotted as function of n (Fig. 2 c). The observed linear relation proofs the validity of the NL model in GICs. These observations obtained from Solin and Nemanich were critical in the study of the Raman response in GICs as they served to distinguish between "outer" graphene layers bounded by intercalants which are highly charged and often called bounding layers, and "inner" graphene layers with little charge and surrounded by other graphene layers also called interior layers in the literature. However, at that time it was not possible to accurately determine the exact charge transfer.

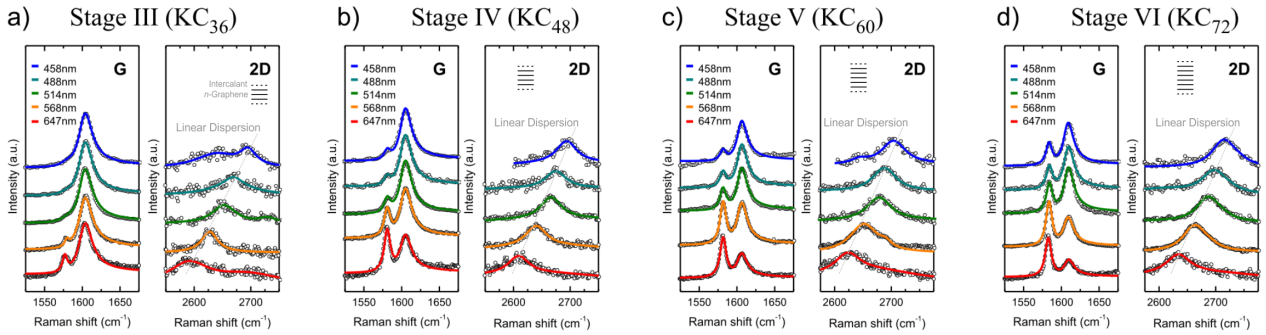

Figure 3 Raman spectra from stage III to VI potassium GIC adapted from the supporting information of Ref. [24]. The different spectra were acquired using laser-excitation wavelengths in the range of (458 nm to 647 nm). In the left panel of a), b), c) and d) the G-line of each intercalation compound is shown; in the right panels of each stage the 2D-line is depicted. The solid lines in the figure are fits using Voigtian and Fano line shapes, respectively. The 2D-line shows a linear dispersion with respect to the laser excitation, and only occurs when $n \geq 3$.

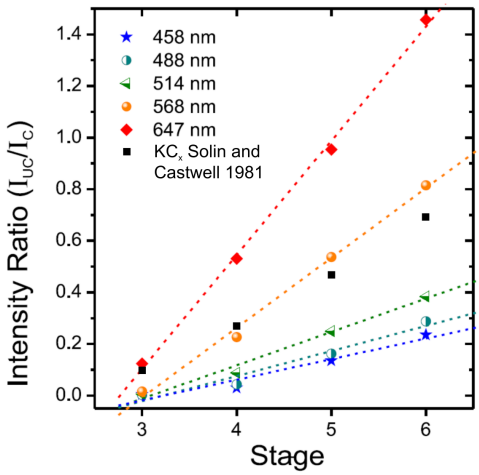

Figure 4 Intensity ratio (R) from the two G-line components in GICs as function of n adapted from Ref. [24]. The experimental intensities extracted from Fig 3 reveal an accurate photon energy dependence of R together with a linear fit of R=I_{uc}/I_c (dashed line) as expected accordingly to the NL model, and the experimental values reported by Solin and Caswell [22].

This highlights that, within the NL model the different stages can be accurately assigned through the relative intensities of the G-lines of inner and outer layers. Hence, the lower-frequency G-line mode in K-GICs around 1580 cm^{-1} corresponds to the G-line of pristine graphite and was therefore ascribed to the inner-graphene layers (supported by the fact that it is absent in stage I and II GICs). The higher-frequency mode around 1610 cm^{-1} present in every stage above stage I was consequently ascribed to outer-graphene layers, even though the exact mechanism of the stiffening remained unclear at the time [17]. Therefore, the NL model itself also has some limitations. It is not sufficient to explain the subtle frequency shifts of the G-line. Furthermore the dependence of the 2D line on staging was not explained. For instance, by taking the intensity ratio R for the stage identification, recent studies showed [24], that this ratio changes as function of the laser energy (see Fig. 3). The linearity of R is conserved, but the slope changes as function of the laser used and needs to be considered (Fig. 4). More over, at that time, the 2D-line had not been studied. As will be shown later, for stages III to VI, the presence of a double resonance Raman process was first studied [24] revealing a linear dispersion with respect to the laser excitation energy .

The final part regarding the effect of intercalation in graphite are the changes in the molecular structure. The inter-planar distance $c = 3.35\mathring{A}$ in pristine graphite tends to be conserved in the interior layers while it expands in the boundary layers. The in-plane arrangement in the graphene planes is similar as in pristine graphite with just tiny deviations to the in-plane lattice constant $a = 2.46\mathring{A}$ and a nearest-neighbor carbon-carbon distance of $\sim$1.42 $\mathring{A}$. The small in-plane lattice expansion due to intercalation in GICs has been explained by Nixon and Parry [26]. The C-C distance change is given by a linear approximation dependent on the reciprocal stage $(1/n)$ as it is shown in Fig. 5 and the following equation:

$$d_{C-C} = (1.4203 + 0.0113/n) \ \mathring{A} \qquad (5)$$

It is important to notice that this linear relation is just valid when $n \geq 3$ and not for highly intercalated potassium compounds as it will be further explained in the applications of GICs (see yellow area in Figure 5). This overall lattice expansion and the absence of superstructure peaks in the XRD pattern are highly important and exclude a phase separation in GICs. I.e., there is no structural difference between the in-plane lattice constant in the

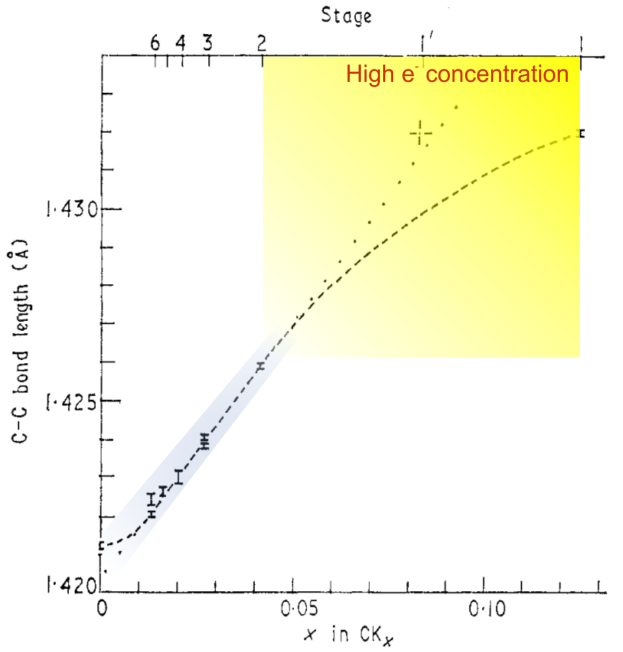

Figure 5 Experimental XRD C-C bond length in potassium GICs adapted from Ref. [26]. The C-C distance from stages I to VI (KC_x) in $\AA$ is plotted as function of their ideal e^- concentration ($1/n$) and their stage index n. The dotted line represents Eq. 5. The yellow region represents the area where electron concentration is higher and the linear model from Eq. 5 fails as stage I does not fit in. The dashed line is just indicative. Reproduced by permission of IOP Publishing. ©(1969) All rights reserved. doi:10.1088/0022-3719/2/10/305

charged bounding layers and weakly charged interior layers.

3 Preparation of GICs As mentioned in the previous section, one of the most important aspects of intercalation is a correct stage determination. This is directly related to the intercalation mechanism. There exist four main routes to carry out intercalation in graphite: i) Two zone vapor transport developed in 1981 by Dresselhaus et al. [2], ii) Electrochemical intercalation, highly interesting since 1970 due to the first lithium/graphite fluoride battery system [27, 28], iii) more recently: Wet Chemical functionalization of graphite which was first introduced to intercalate carbon nanotubes [29–31] and further on adapted for graphite [32, 33] looking for bulk productions of graphene, iv) in-situ intercalation by vapor transport and subsequent annealing in UHV and HV environments [7]. The latter is an adapted version of the two zone vapor transport method.

3.1 Two-zone vapor transport method The preparation of GICs has never been trivial as it is not easy to control the proportions of intercalant and keep them constant along the measurements. Since 1980's intercalation has been made using the *two-zone vapor transport method* (see Fig. 6 a) [2]. The principle of this method consist in heating up the intercalant to a desired temperature T_i, while the graphite (some distance away) is also heated to a temperature T_g. The difference in temperature determines the expected intercalation stage as depicted in Fig. 6 b). At this point it is important to consider the stability region for each stage. For instance a stable stage I face exist at ΔT<100^{o}C, while stage II can be reached with a ΔT between 100 and 200^{o}C. By enlarging the temperature difference, higher stages going from III to n can be reached. However, when stabilizing and synthesizing line phases of highly staged GICs this method is getting more complicated as there exists no plateau ΔT for the individual stages. When intercalation with alkali-metals like potassium occurs, an evident change in color from the graphite can be observed, which has been used as a bench mark for a proper stage determination. For instance a yellow, gold or red color is characteristic of stage I compounds, and steel blue for stage II, dark blue for stage III and graphite-metallic for higher stages.

In the case of acceptor compounds stage I is often blue and higher stage compounds are graphite-metallic colour [9]. Typical examples can be seen in Fig. 7 where six optical images from the same region acquired with a 100x microscope objective during intercalation/de-intercalation denote a mixture of stages in the same graphite HOPG sample [7]. In panel a) the golden color of highest intercalation stage I (KC_8) is shown. However, one can clearly observe that the bulk sample is not homogeneously intercalated which means that it has several crystalline domains in the HOPG and the presence of differently intercalated regions like a stage II phase (KC_{24}) in the lower right side of the picture. As we move forward with de-intercalation in Fig. 7 panels b) to f), it can be seen how the sample change in color from yellow/golden to red, then green and further brown-green. This color inhomogeneity is an indication about the stability from each isobaric growth phase in potassium GICs. The actual color observed is slightly modified by the reflection of the lamp in the microscope and interference effects in partially intercalated crystallites. This also means that a particular color is absorbed by the sample, and our eyes observe the complementary color coming from the mix of the residual light wavelengths as has been also proven by reflectivity studies [34]. In this studies the Drude-like free-electron spectra for light polarized parallel (blue) and perpendicular (black) to the c-axes in GICs had been recorded. Due to the intercalation, graphite behaves like a metal exhibiting a sharp Drude edge in reflectivity [35] and a Drude peak in Electron Energy loss spectroscopy [36–38] of a screened charge carrier plasmon in the visible region with a Drude minimum around 2.6 eV and a directly observed Drude peak in EELS of about 2.3 eV for KC_8, and 1.8 eV for KC_{24} (Stages I and II). These screened plasma frequencies

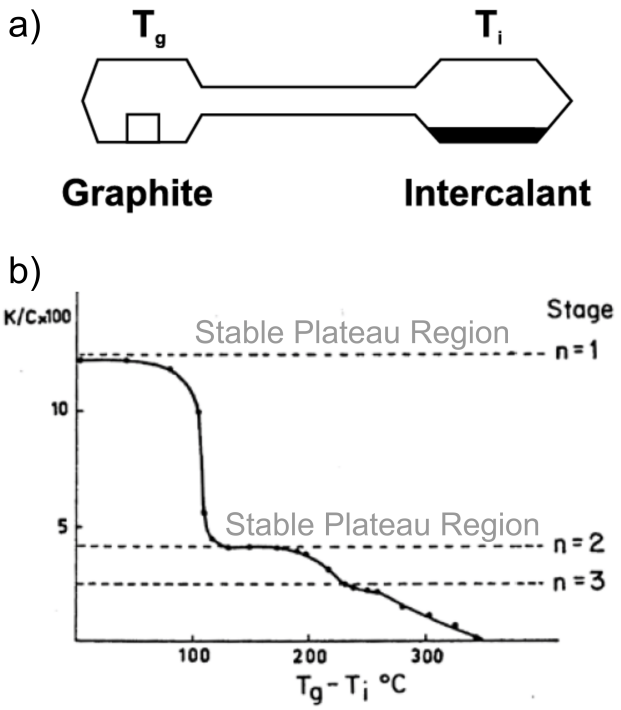

Figure 6 Two-zone vapor transport method from Ref. [2] a)Schematic diagram of a sealed ampoule with two-zones, where T_g, and T_i indicate the temperatures of graphite and intercalant respectively. b) Isobar graph for growing conditions in graphite-K compounds. Reproduced by permission of Taylor & Francis Ltd. Publishing. ©(1980) All rights reserved

$omega_p$ of the free charge carriers are largely responsible for the characteristic color in highly intercalated GICs.

Another important factor to mention is, that GICs are extremely sensitive to oxidation in ambient conditions. The success of the *two-zone vapor transport method* is also related to the fact that all synthesis is happening in sealed ampoules, i.e. avoiding air at any time. However, further experiments after removing from the ampoule, even in the best Glove box might lead to a contamination, de-intercalation and oxidation of the surface. This is the reason why this method is not accurate enough for surface sensitive methods like photoemission where in-situ UHV intercalation has been applied. More recently the use of new *in-situ* systems (process iv) in high-vacuum Raman doping cells allow the possibility to have a well controlled and consecutive *in-situ* intercalation [24, 39] with an accurate stage determination in a systematic manner.

3.2 Electrochemical intercalation Electrochemical doping or intercalation provides an alternative way to modulate the Fermi level of graphene [41]. The later is an attractive application towards field-effect transistors (FETs). Additionally, in contrast to electrostatic doping [42], not so high voltages (∼1.5 V) are required in order to achieve considerably high doping levels.

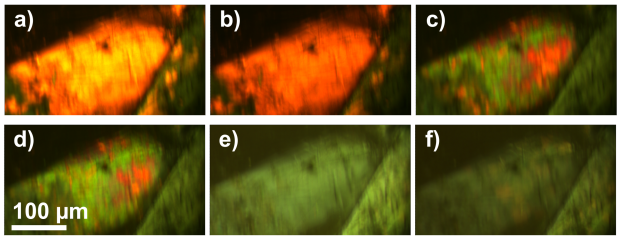

Figure 7 Micrographies of the change in the crystal color according to the content of potassium adapted from Ref [7] (Multi-crystalline HOPG). a) Mixed KC_8 and KC_{24} regions, b) Defective KC_8, c)-d) Mixed KC_{24} and defective KC_8. e) Homogeneous KC_{24}, and f) Mixed KC_{24} and defective KC_{36} faces (see also Ref. [40])

Graphite intercalation compounds under electrochemical intercalation have been produced with the aim of improving batteries [27, 28]. This process involves graphitic electrodes immersed in an electrolytic solution with a chemically and mechanically stable host (graphite in this case) which acts as a breathing matrix where ions can be sucked-on and in a discharge process the charge can be expelled-out. GICs are primary candidate for this process as a secondary cathode and Li GICs as well as Li intercalated nanotubes are used in Li ion batteries [43, 44]. Recently, in-situ Raman and transport studies upon electrochemical doping have been also applied to extend the doping range to much higher levels in field effect doping via the use of nanometer-thick solid polymer electrolytes gate which provides a much higher gate capacitance than the regularly used SiO_2 back gates in FETs [45, 46]. These experiments have shown (in agreement to the *two-zone vapor transport method*) a splitting of the G-line with doping.

Even if high doping levels can be achieved with this method, the need of an electrolyte for the doping limits its possibilities to apply surface sensitive techniques. The intrinsic charge transfer between the intercalant and the host generates two typical reactions in the graphitic electrodes and the aprotic solutions which lead to salt-like lamellar graphite compounds, which for instance may lie in the observed Raman response and/or a deterioration of the intercalation compound. Moreover, an indispensable condition for these two reactions is, that the carbon material employed must be a well orientated graphite. This illustrates, that a deterioration of the host lattice, originating e.g. from cycling the electrode, affects the overall chemistry [27, 28].

Similar response of the G-line has also been observed in Raman spectroelectrochemistry of bilayer $^{12}C/^{13}C$ graphene [41]. In that work, a subsequent bilayer graphene was made by depositing a ^{12}C graphene-layer on top of a ^{13}C graphene-layer on a SiO_2/Si substrate. The Raman analysis showed a split of the G-line assigning the contribution of the low-frequency mode to the ^{13}C graphene

and the high-frequency mode to the ^{12}C layer [41]. The use of Raman spectroscopy as a tool to identify single graphene layers contributions was evident. The deviation in frequency from the two G-line components uncovered the difference in masses from ^{12}C and ^{13}C graphene. In addition, Kalbac et al. found an effect of the substrate to the boundary graphene layer which stressed in comparison to the outer one. Finally their study also revealed a weak electronic coupling between graphene layers which served to explain their G-line intensity difference. The last points bring an insight of using Raman spectroscopy as a tool to study charge transfer and stress in graphene, as will be confirmed in the following section.

4 Using Raman spectroscopy to understand charge transfer and structural changes in GICs: Application potential and organic Superconductivity Turning into the possible applications of GICs, Dresselhaus [2] pointed out that GICs have not been widely used for industrial applications, whereas graphite is an extensively used industrial material which offers the possibility to combine them both and bring new commercial applications. Inagaki [47] at that time also pointed out that GICs stand out from other materials due to their high electrical conductivity, and they exceed as electrodes for primary and secondary batteries with an easy diffusion of electrochemically active species between the graphitic layers. This lead to the above mentioned application in Li ion batteries [48–50].

GICs can also be used to exfoliate graphite prepared by rapid heating of GICs leading into a bulk production of graphene sheets which may be promising for industrial applications [32]. However, there are still many problems to be solved in order to achieve all these as commercial applications. For instance, one must properly control the intercalation process, and make GICs stable under ambient conditions. The later relates to stage I GICs which is a material that shows superconductivity. This organic superconductivity in GICs and the possibility to get a material with a reasonably high transition temperature that can be tailored by the choice of intercalant has always been one of their most interesting aspects, both from the basic science point of view, as well as for future applications. For electron phonon coupling based BCS superconductivity stage I GIC combine two very promising ingredients, i.e. a high phonon frequency and a high electron phonon coupling constant (EPC).

In this section we will give a brief summary how Raman spectroscopy can give important insight towards accessing these applications. In the first subsection a brief overview on how Raman spectroscopy can contribute to understand the EPC in stage I GICs is presented. This will also be compared to complementary studies on intercalated fullerenes, intercalated nanotubes and doped graphene. In the second subsection we will focus on how to use Raman spectroscopy as a nondestructive key tool to disentangle the effects of charge transfer and strain in highly staged GICs and its importance for determining the local interfacial strain and the internal charge transfer in charged and strained graphene.

4.1 Superconductivity in stage I GIC and implications for intercalated fullerenes, nanotubes and doped graphene Superconductivity in GICs was first studied by Henning and Meyer in 1952 [51]. Later on, Hannay and Kobayashi1 [52, 53] were able to extract the superconducting transitions for first stage GICs with K, Rb and Cs as intercalants. The first superconducting graphite intercalation compound to be reported was stage I KC_8 [2, 52, 54]. The transition temperatures reported for GICs at that time were low in the range of 0.135 K for CsC_8, and between 0.39-0.55 K for KC_8 [2]. The case of LiC_6 did not show any superconducting behavior, whereas the metastable high-pressure LiC_2 compound revealed a "high" T_c of 1.9 K [55]. By 1990's higher transition temperatures were observed for C_6K, C_3K, and C_2Na with values of T_c = 1.5, 3, and 5 K respectively [56]. In 1991, the discovery of fullerene intercalation compounds known as "fullerides" added a new family of organic superconductors [57–59]. Fullerides revealed higher T_c values compared to GICs ranging from 18 K for K_3C_{60} up-to 39 K for Cs_3C_{60} [58–60]. In 2007 Hlinka et al. discovered superconductivity in CaC_6 GICs with an elevated T_c of 11.5 K [61] renewing the interest in graphite intercalation compounds. Superconductivity in CaC_6 has not been fully understood yet. Some studies attribute this effect to the high energy C modes [62], while others [63] report that the low-energy modes of the intercalant were responsible for superconductivity inferred from specific heat analysis. First-principles calculations predicts equal coupling to both groups of phonons [64, 65]. The origin of superconductivity in GICs is still a controversial topic [64, 66–68]. One of the most accepted theories relates the electronphonon interaction both to Ca and C vibrations [64] which should be measurable by resonant Raman spectroscopy of stage I GICs.

Raman spectroscopy has been served as a central tool in the analysis of the superconducting coupling mechanism in GICs. [7, 10, 61, 69]. The resonance Raman spectra from stage I superconducting GICs shows the strongest vibrational mode as a Fano line-shape around 1510 cm^{-1} [17,70,71] for KC_8 and CaC_6, not like in LiC_6 (see Fig. 8 a). The previous highlights the importance of this Fano-interference to the superconductivity coupling mechanism within the BCS theory, and confirms the importance of this E_{2g_2} G-line mode to non-adiabatic effects.

The correct assignment of the intrinsic Raman response in superconducting stage I GICs is especially important since superconductivity is based on electron phonon coupling (EPC) involving the graphitic E_{2g_2} G-line phonons [72, 73] and the renormalized position and line-width of these modes can serve to calculate the EPC constant in the superconducting GICs [69]. Early studies

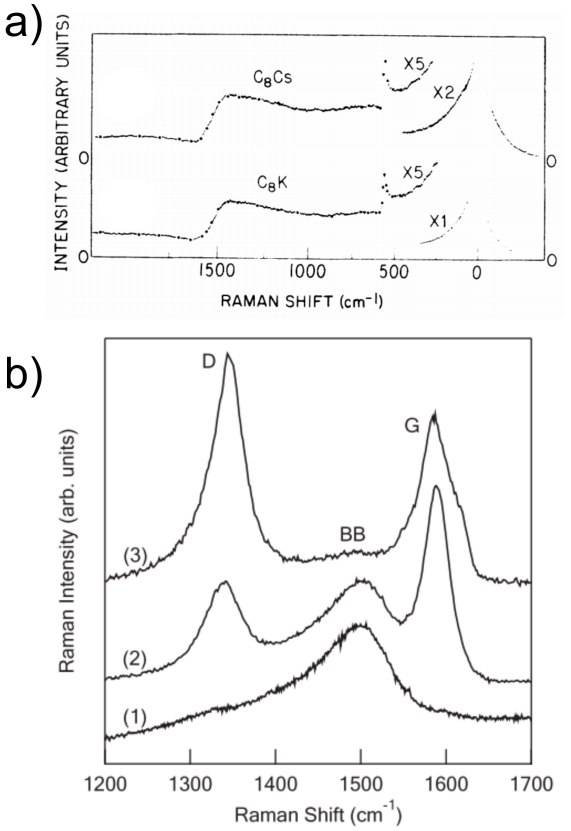

Figure 8 Raman line-shape analysis for K, Ca, and Cs stage I GICs, adapted from Ref. [21] and [61] a) KC_8 and CsC_8 characteristic Fano line-shape at high doping concentrations. Two main components are depicted the main G-line component around 1510 cm^{-1}, and the C_z-mode at $\sim$550 cm^{-1} due to the inter-planar lattice vibrations. b) CaC_6 Raman spectrum, from where the bottom spectra refers to the not air exposed sample, while the others are air exposed after several hours. Disorder and de-intercalated peaks reveal the decomposition of the sample. Reprinted figure a) with permission from R. J. Nemanich, S. A. Solin, and D. Güerard, Phys. Rev. B 16, 2965, 1977 ©(1997) by the American Physical Society. Reprinted figure b) with permission from J. Hlinka, I. Gregora, J. Pokorny, C. Hérold, N. Emery, J. F. Marêché, and P. Lagrange, Phys. Rev. B 76, 144512, 2007 ©(2007) by the American Physical Society.

in single walled carbon nanotubes (SWNTs) intercalated with potassium introduced the use of a Breit-Wigner-Fano (BWF) component to explain the Raman features around 1500 cm^{-1} [74]. This mode was proven to exist in bundles of SWNTs intercalated with potassium, and explained as a hybrid plasmon-phonon mode derived from a plasmon band that reduces the phonon excitation required to generate the BWF mode [75]. The latter is critical in the study of GICs as the E_{2g_2} G-line mode in stage I superconductivity compounds also depict a BWF line-shape [70].

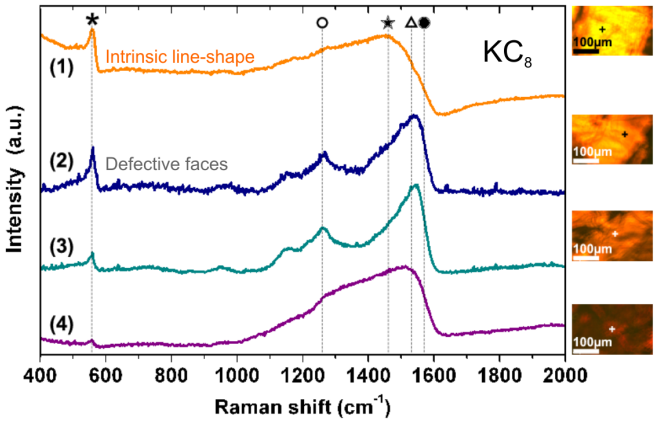

Figure 9 Raman spectra of four different KC_8 single crystals (labeled 1 to 4 and assigned by their color) adapted from Ref. [40]: (1) highly bright and golden crystal, (2) low bright golden crystal, (3) red crystal, and (4) red to black crystal. The symbols denote: $*$ $\mathbf{C}_Z$ mode, $\circ$ **D** mode, $\triangle$ E_{2g_1} mode, $\star$ E_{2g_2} mode, and the $\bullet$ **GD** mode representing the characteristic de-intercalation component from Stage I to II. The orange top-line represent the intrinsic Stage I face in GICs without defects along an homogeneous region. Reproduced by permission of John Wiley and Sons Publishing. ©(2011) All rights reserved.

In order to correctly extract the Raman response of superconducting stage I GICs many factors must be considered such as intrinsic disorder of the crystal, laser induced heating of the sample, and air intrusion strongly affect the Raman response in GIC. An example of the latter can be depicted by different experimental and theoretical studies reported with a wide range of different G-line positions and line-shapes between $\sim$1400 cm^{-1} and $\sim$1600 cm^{-1}: i.e. at $\sim$1500 cm^{-1} [2], between 1400 cm^{-1} and 1550 cm^{-1} [17], 1534 cm^{-1} [69], 1547 cm^{-1} [21], 1420 cm^{-1} and 1582 cm^{-1} [76]. The incongruity of these results is directly related to an incomplete intercalation as reported recently in potassium doped graphene [12] and stage I GICs [70]. On top of this, defect modulation of GICs is crucial when studying the G-line response from superconducting GICs faces. For instance, Hlinka [61] reported different G-line positions and line-shapes for CaC_6 exposed to air (see Fig. 8 b), which is in contrast to the fine BWF line-shape observed by Nemanich et. al. in Fig. 8 a) for K and Cs GICs. A recent study, on stage I single crystals of KC_8 (see Fig. 9) [40] revealed that this differences are related to local defects and different intercalation and laser induced de-intercalation. This can be clearly seen in the Raman spectrum, which changes as function of the quality of the crystal and different Raman modes appear. This will be described in the detail in the following.

The peak labeling in stage I GICs is not a trivial work. As it has been demonstrated by Hlinka et al. [61] and

Dean et al. [72], recent Raman spectroscopy studies of highly intercalated GICs (i.e. stage I, II) present several components in the G-line region (see Fig. 8). In accordance with these studies, additional works have covered a detailed line-shape analysis as depicted in Fig. 9 revealing four components. The first and last component have a Lorentzian line-shape whereas the ones located around 1500 cm^{-1} keep a BWF line-shape. These lower and higher frequency Lorentzian modes are labeled as D and GD in the Figure and they are attributed to intrinsic defects present in the sample [40, 72]. The latter GD component has been further studied in Refs. [70, 77] and the origin of the GD mode has been recalled as the contribution of not fully intercalated defective stage II regions embedded in stage I GICs. This is in agreement to the fact that this mode is not dispersive, and to the Daumas-Hérold model [23] which predicts that multiple stages may coexist in the same system.

We turn now to the intrinsic Raman G-line response of the stage I compounds, which had been very controversial in the previous literature. Following the line shape analysis, the two strongest components around 1500 cm^{-1} have been labeled as E_{2g} modes [2, 40, 61, 70, 72, 77]. These modes belong to the in-plane stretching vibration of the carbon atoms. In GICs the Brillouin zone of graphene folds back allowing to have Raman active E_{2g} modes whereas the A_{2g} mode became silent. The first E_{2g_2} mode change in frequency and line-shape as function of intercalation [2, 40, 61, 70, 72]. For stage I GICs this mode shows a BWF line-shape, which for KC_8 locates at 1510 cm^{-1}. In addition, the second strongest mode is assigned to the E_{2g_1} vibration because it is in the same frequency range. However, this mode is observed as the second high frequency BWF mode around 1547 cm^{-1} with a different origin. It is related to the recombination of one E_{1u} mode and one of the E_{2g_2} modes [78]. Therefore this component is not related to the intrinsic G-line of stage I GICs.

Another important factor in the correct analysis of the G-line of stage I GICs is the temperature of the sample (T). Raman spectroscopy analyses on CaC_6 [79], and LiC_{12} [80] had been made at low-T, but much less is know about them. These Raman reports have been performed bellow the Tc of CaC_6, and at 240K for Li GICs. The results showed reversible transition phases and the appearance of peaks not present at room temperature (RT) related to in-plane vibrations around 40 cm^{-1} [79]. In the case of LiC_{17}, it shows a doublet G-line assigned to the presence of LiC_{17} and LiC_{18} phases. The latter works revealed some important facts: i) Low-T Raman analyses in GICs may enhance the observation of different vibrational modes in their structure, ii) The possibility to distinguish between interior and boundary-layers is much more evident through low temperature Raman studies, iii) the line shape analysis of the G-line with more than one component agrees the studies in defective stage I GICs [70, 77], iv) Low-T Raman analyses change the ordering of the molecular structure in GICs allowing to have mixed intercalation phases within the same crystal as predicted by the Daumas-Hérold model [23], and finally v) There exist a need of a systematic low temperature Raman study about stage I GICs to fully understand their superconducting behavior and perhaps its EPC mechanism.

Some studies have revealed that by determining the frequency of the E_{2g_2} G-line mode, one can extract the line width $\gamma_\sigma^{EPC} = \Gamma$ [10, 61, 69, 70, 81] especially for CaC_6 (see Fig.10). Thus, from the Raman spectra in GICs one can learn in fact the contribution from the highest optical mode which originates from extremely high doping levels and how this contributes to the EPC constant responsible for superconductivity in stage I GICs. However, the contribution of this optical phonon to the electron-phonon coupling constant (λ) is not enough to explain the high T_c in GICs [70, 71], as it has also been attributed to the in-plane TO phonon from the K point as analyzed from the kink in the quasi-particle dispersion from the ARPES results [82]. It has also been shown that the major contribution to λ in superconducting GICs comes from the low-energy modes and the carbon vibrations along the z-axes [83, 84]. A full analysis of KC_8 reveals an EPC of $\lambda = 0.45$ [82]. This is bigger as compared to the EPC derived from Raman spectroscopy alone.

Additionally, stage I GIC behaves like heavily doped graphene. It follows an AA stacking order and allows to unravel the truly experimental Dirac cone [85]. For instance, even if superconductivity is not depicted in the bulk, that does not mean that it can not be achieved at the mono-layer. For example, by considering stage I LiC_6 GIC a complete charge transfer occurs between the Li atoms and the graphene layers, whereas the removal of quantum confinement in mono-layer graphene doped with lithium can up-shift its interlayer state and induce superconductivity as found to be for LiC_6 mono-layer graphene and Li_2C_6 with T_c=8.1 K [83] and T_c=18 K [84]. Therefore it is obvious to correlate these results to results on alkali-metal doped quasi freestanding graphene and address its EPC and estimate their contribution to high temperature superconductivity. This will be briefly summarized below.

Quasi free-standing doped-graphene has first been confirmed by Angle Resolved Photo-emission Spectroscopy (ARPES) in stage I KC_8 as a key to study graphene [85]. It has been shown that the inter-layer spacing between layers in GICs can be increased (due to intercalation) from 0.34 nm (3.4 $\AA$) in pristine graphite to more than 1 nm in some GICs exaggerating the anisotropic properties of graphite [2, 50]. The previous also bring a significant reduction in the van der Waals forces between adjacent graphitic layers, which leads into a new route to study single layers of graphene from a top-bottom approach [50, 86, 87]. Graphene, "the mother of all graphitic forms" [88], is considered the building block for every sp^2

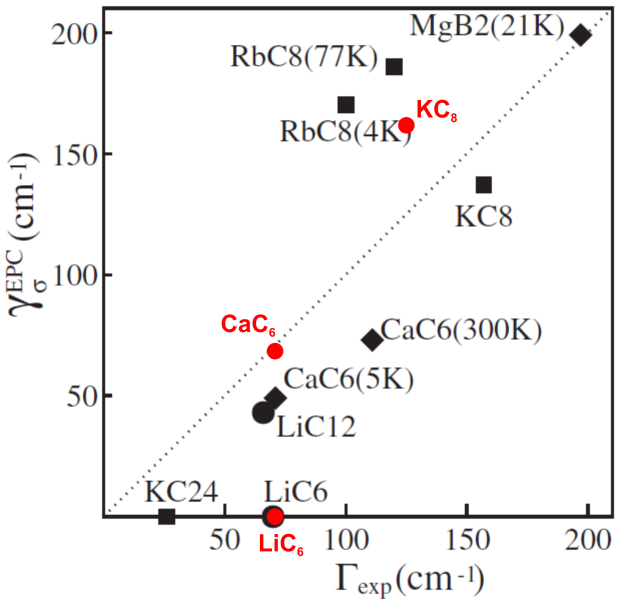

Figure 10 Calculated and experimental EPC line-widths adapted from Ref. [69]. The black squares and circles represent the values reported in Ref. [69], while the red dots depict the experimental values extracted from the Raman response in Stage I GICs from Ref. [70]. Reprinted figure with permission from A. M. Saitta, M. Lazzeri, M. Calandra, and F. Mauri, Phys. Rev. Lett. 100, 226401, 2008 ©2008 by the American Physical Society.

hybridized carbon allotrope. The importance of graphene lies in its exceptional electrical [89, 90], thermal [91], and mechanical [92] properties. Graphene then attracted high interest in various fields of applications [93] like: field-effect transistors (FETs), sensors, electrochemical capacitors/super capacitors, lithium ion batteries (LIBs), fuel cells, and solar cells. All of these properties directly relate to the low-energy electronic structure of graphene [88,89]. ARPES has been proven to be a key tool to determine the electronic structure of graphene [94] and graphite [95–97].

The major problem to deal with when analyzing graphene is the direct hybridization between the substrate and the graphene layer, which for instance can modify the electronic structure due to charge transfer effects [98–100]. A way to circumvent the problems of substrate-interaction effects was the use of potassium intercalation. One can see, for instance, stage I KC_8 compounds as a quasi free-standing graphene layer laying on top of every single potassium interlayer [85]. In a similar way, it was shown by *in-situ* ARPES measurements and *ab-initio* calculations [85] that the electronic properties of intercalated graphite and graphene are equivalent. This allowed to observe for the first time the Dirac cone of doped graphene experimentally by using KC_8 GICs, in contrast to previous works where the substrate induced a gap opening [99] or where the Dirac point was not really visible because it was lying at the Fermi edge. The equivalence of KC_8 GICs and graphene was revealed by the dispersion of the electronic bands which is not different from the dispersion of bands in graphene close to the Dirac point. This demonstrates the existence of noninteracting doped graphene layers in the molecular structure of GICs and provides an elegant solution for the study of graphene.

More recently, alkali-metal intercalation in graphene has served as a tool in determining the size of the EPC from the analysis of the kink in the quasi-particle band structure. Using the full phonon density of states, electronic dispersion and the Eliashberg function, a very strong electronphonon coupling constant could be determined [101]. This could induce superconductivity at elevated temperature in graphene. They determined the quasi-particle band structure in ARPES (see Fig. 11 a), b) for K-doped graphene) and the EPC λ (see Fig. 11 c) to evaluate the superconducting critical temperature T_c from graphene intercalated with Cs, Rb, K, Na, Li, and Ca. The latter has been done by performing ARPES analysis of graphene to extract the EPC as a kink from the spectral function resulting from the sample. This work bring an insight in the study of graphene doped/intercalated with alkali-metals revealing that the EPC constant that comes from graphene's high energy phonons alone is too low to sustain superconductivity, in agreement to previous works on Raman GICs [70]. In the case of Raman spectroscopy, the EPC constant extracted from the highest optical phonon in Stage I GICs is also too low to explain superconductivity leading to an open question regarding the phonons responsible for this behavior.

This experimental relation of the coupling constant and the coupling phonons [70, 82] to the superconducting transition temperature is based on a classical BCS coupling theory via phonons and has been theoretically predicted through several studies. For instance, Saitta et al. [69] have proven that by extracting the electron phonon coupling constant λ from the electronic and phononic structure one can empirically estimate the critical temperature of superconducting KC_8, and CaC_6. In 2012, Profeta et al. [83] theoretically demonstrate the possibility to induce superconductivity in graphene by doping its surface with alkali-metals like done in GICs, revealing that Li-covered graphene superconduct at higher transition temperatures (8.1 K) than the ones they obtained for Ca-covered graphene (1.4 K). In addition to the latter, the EPC can be strongly enhanced by the coupling between out-of-plane graphene phonons and in-plane intercalant [64, 68, 102]. The intercalation of bi-layer graphene would enlarge the resulting T_c for this systems as the carbon-intercalant ratio gets lower and axial z-vibrations between graphene layers exist. These assumptions have been proven by C_6CaC_6 (bi-layer graphene) with a T_c close to the one of CaC_6 [103]. In addition, Ca does not present an ordered phase when deposited onto monolayer graphene in contrast to bilayer graphene. The latter highlights the

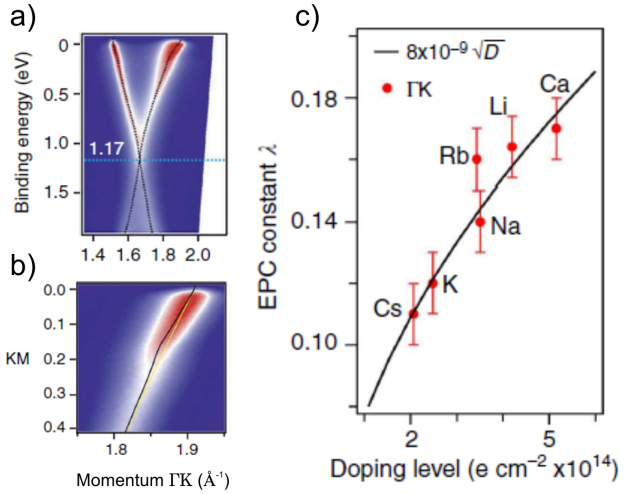

Figure 11 Experimental ARPES intensities of potassium doped graphene [101]. a) K-doped graphene spectra along the ΓKM direction near the K point at 1.7 $\AA^{-1}$ b) High resolution ARPES along the KM direction depicting the kink to extract the EPC constant λ. c) EPC constant for different alkali-doped graphenes extracted from the high-energy optical phonon modes only with respect to their corresponding electron concentration. Adapted by permission from Macmillan Publishers Ltd: Nature Communications [101] © 2014.

importance of intercalation to achieve ordered phases of intercalant with pairing coupling constants similar to the bulk graphitic compounds [101, 103].

In the following we will compare for completeness these results with respect to superconductivity and the gain from Raman spectroscopy to other nanocarbon based intercalation compounds, namely fullerene intercalation compounds and intercalated nanotubes.

Superconductivity in fullerene intercalation compounds and intercalated nanotubes have been an obvious next step because of the ability of fullerene single crystals and single walled carbon nanotube (SWCNT) bundles to occupy alkali metal counter ions in their open voids. However, for fullerenes in contrast to graphite and carbon nanotubes a p-type doping was not possible so far because of the low electron affinity. In 1991 the first intercalation compounds with fullerenes (fullerides) where elaborated [57–59, 104] the same way as performed in graphite intercalation compounds. The excitement of using these new material at the time was promoted by the possibility to achieve higher transition temperatures for superconductivity, and the introduction of dopant ions into the crystal without disrupting the bonding environment in the fullerene sphere generating a tri-dimensional isotropic organic conductor [58]. In addition line phases are observed with a metallic and superconducting phase for alkali metal doping of A_3C_{60}. Similar to oxide based high temperature superconductors this phase is on the borderline of a metal insulator transition. For different fullerene intercalation compounds the detailed interplay between electron-electron and electron-phonon interactions leads to different ground states of a superconductor (i.e. Cooper paar formation via EPC in agreement with the BCS theory), charge transfer insulator (i.e. via Jahn-Teller distortion) and Mott-Hubbard insulator (i.e. via electron electron correlation) as reviewed in Ref. [105]. Raman spectroscopy has been used as key tool to identify the line phases in fullerene intercalation compounds utilizing the linear red shift of the A_g pinch mode with doping [106–109], as well as the EPC of the H_g-derived coupling modes [109]. In comparison to classical superconductors, and in contrast to GICs the T_c observed in fullerides is much higher ranging from 18 K in K_3C_{60}, 28 K for Rb_3C_{60}, and up to 39 K for Cs_3C_{60} which is the record transition temperature for organic superconductors so far [58–60].

Coming to the study of superconducting single walled carbon nanotubes (SWNTs) no line phases but rather a continuous doping had been observed [110]. This makes it much harder to observe the correct stoichiometry related to superconductivity. Also there are theoretical studies related to superconductivity in doped SWCNT [111] experimental studies are rare for intercalated SWCNT. Superconductivity in B-doped SWCNT was claimed to be up to a T_c of 12 K [112], for SWCNT in zeolites a T_c of 15 K was shown [113].

Further effects derived from the intercalation of chemical species in between the basal graphene layers in GICs have lead not only to superconducting effects, but also intrinsic charge transfer and induced strain within the graphene layers. In the following we will present how these effects have been observed and serve as new tool when studying doped and/or strained graphene based systems.

4.2 Raman study of charge transfer and strain in highly staged GICs – implications for doped graphene: Charge transfer, hybridization and strain are intrinsic effects in graphite intercalation compounds. Here we will give a detailed study of the interplay between these effects in higher stage GICs (above stage II) beyond the limitations of the NL model. For this purpose we introduce the above mentioned graphene bounding layers adjacent to the intercalant as charged (c), and interior graphene layers with only graphene nearest-neighbor layers as uncharged (uc).

The first studies on charge transfer in GICs have been theoretical calculations used to disentangle the fractional electronic charge f being transferred from the intercalant atoms to graphite [114]. These studies focus on the explanation about charge distribution among graphene layers in the whole compound where boundary and interior layers co-exist in the system. This coexistence is only possible in intercalation stages $n \geq 3$, as in stage I and II every graphene layer is adjacent to an intercalant layer. These studies were computationally expensive because large

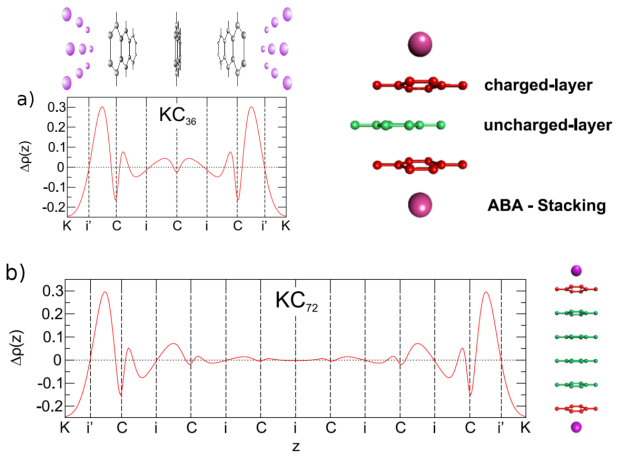

Figure 12 Theoretical Charge Density Distribution adapted from Ref. [24]. a) Stage III KC_{36} with a sketch of the charged and uncharged layers and its corresponding charge distribution along the z-axes. The position of the carbon/potassium planes is marked by C/K. The midpoints graphene planes are marked by i and the separation between K and C atoms is marked by i', here the density difference crosses $\Delta\rho = 0$ b) Charge distribution analysis for KC_{72} depicted in the same way as in a).

supercells must be used to represent systems like KC_{36} GICs [115].

Early results from *ab-initio* calculations in stage I GICs intercalated with Li, Na, K, Rb, and Cs [115] revealed a "nearly constant" charge transfer from the alkali-metal to the graphene boundary layer (charged layer) and established a proper way to exemplify the charge transfer mechanism in GICs. Ancilotto and Toigo [116] developed a 2x2 supercell geometry from which they revealed an incomplete charge transfer from K atoms into the graphene boundary layers, and were able to overcome the problem of supercells when analyzing GICs. Their results served as the first step in the understanding of alkali-metal graphite interactions, but called for a more quantitative study in the future. More recently, a combined Raman spectroscopy and *ab-initio* calculation study [24] in low intercalation stages (III-VI) brought a quantitative description of the charge transfer mechanism in GICs by following the Hartwigsen method [115] on stage I GICs and by Ancilotto and Toigo [116] on potassium adsorption in graphite. For that purpose, the charge density difference ($\Delta\rho(z)$) must be calculated considering the charge density from the whole GIC minus the reference one ($\rho_{ref}(z) = \rho_{graphene}(z) + \rho_K$) [24].[1]

Table 2 Calculated charge transfer (e^- per K atoms) from the intercalated K atoms to the graphene-layers for *stage III* to *VI* potassium GIC taken from Ref. [24]. The last column gives the bi-axial strain of the graphene layers [26].

	el. per K atom				σ (10^{13}/cm^2) *			Bi-axial strain (%)
	K	1st	2nd	3rd	1st	2nd	3rd	
KC_{36}	-0.39	0.33	0.12	-	5.2	1.9	-	0.20
KC_{48}	-0.39	0.28	0.11	-	4.5	1.7	-	0.13
KC_{60}	-0.39	0.26	0.11	0.04	4.1	1.7	0.6	0.10
KC_{72}	-0.39	0.26	0.10	0.03	4.1	1.6	0.5	0.06

* The corresponding electron density is given in electrons/cm^2.

The latter calculated results are shown in Fig. 12, where stage III KC_{36} (a) and stage VI KC_{72} (b) are shown. For the first time, a complete quantitative charge transfer distribution was obtained for stages III to VI depicted in Table 2. The results highlight the accumulation of electrons in the boundary carbon layers with constant values independent of the stage. In contrast, the charge transferred to the interior layers decreases and varies as function of the stage.

A secondary effect of charge transfer in GICs is the splitting of the G-line in two when the stage index $n \geq 3$ [26]. The G-line in stages III to VI shows a high frequency and a low frequency mode [2, 24]. The first one has been assigned to the vibrational Raman response of the charged graphene layers next to an intercalant one, whereas the low frequency one corresponds to the uncharged or slightly charged graphene sheets. Their positions are ~1602 cm^{-1} and ~1580 cm^{-1} respectively. The previous assignment can be observed in Fig. 13 a) and explained in the following way:

–**High-frequency Gc mode:** It is located between 1600 and 1610 cm^{-1} (Fig. 13 b, red line). This peak is slightly asymmetric due to a Fano interference of the conduction electrons transferred from the potassium to the charged graphene layers. This is also supported when comparing the Raman response of stage II KC_{24} where only charged graphene layers boundary to intercalant exist. Therefore, KC_{24} exhibits only a Gc-line at 1610 cm^{-1}. The strong up-shift in position of the G-line in graphene due to electron-doping (charge transfer) has been explained [118] as a breakdown of the Born-Oppenheimer approximation for the E_{2g2} phonon mode at Γ. Comparing to experiments

[1] Calculations have been performed using density-functional theory (DFT) in the local-density approximation (LDA). The Quantum-espresso package [117] has been used. Since DFT does not yield reliable inter-plane distances, calculations were done at the experimental C-lattice constants of Eq. (4). The carbon-bond lengths were taken from the experiments by Nixon and Parry [26]. DFT is known to be problematic in the calculation of charge-transfer processes. Yet, in the case of K intercalation of graphite, it reproduces at least qualitatively correctly the tendency of the potassium atoms to give away their electron to the graphite host. Since the accumulation of charge on the boundary layers is determined by the electrostatics of the system, we assume that the charge-density plots (in particular the comparison between the different stages) are at least qualitatively correct. The absolute amount of the transferred charge density remains a challenge for DFT.

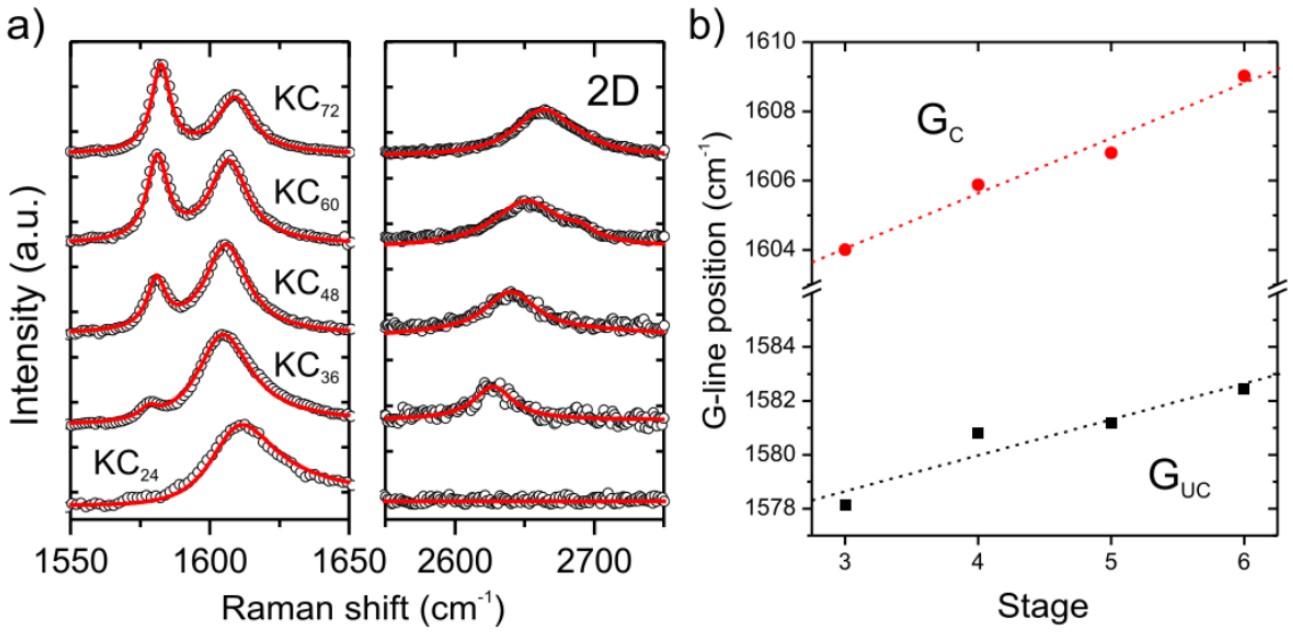

Figure 13 Raman spectra of the G- and 2D-line regions from stage II to VI GICs acquired at 568 nm in Ref. [24]. Panel (a) depicts experimental results (black dots) and line shape analysis (red line) results revealing the presence of a split G-line and a 2D component for stages III–VI. Stage II shows just one asymmetric G-line peak and no 2D mode. Panel (b) revealed a linear increment in frequency from the two G-line components (Gc and Guc as a function of stage n).

performed on electrochemically top-gated graphene where doping with electron concentrations of about 5x10^{13}/cm^2 (similar to the ones in Table 2) lead to a G-line at around 1605 cm^{-1}, we conclude that the strong up-shift of the Gc-line is indeed due to charging of the graphene layers adjacent to the intercalant.

–**Low-frequency Guc mode:** In addition, for stages higher than KC_{24} a second G-line (Guc) came out at ∼1580 cm^{-1} (Fig. 13 b) black) being close to the G-line position of pristine graphite and graphene (1583 cm^{-1} and 1580 cm^{-1} respectively [98]). Thus, the Guc peak is assigned to pristine uncharged graphene layers with a symmetric Lorentzian line-shape in GICs [24]. In order to confirm the origin of this Guc-line in GICs, one must consider the slight charge transferred to the interior layers in GICs as depicted in Table 2. The frequency values that one can obtain by taking σ from Table 2, and Eq. 3 from Ref [119] overestimate the ones observed for stages III to VI in GICs [24], which means that additional factors must be considered in order to match the experimental values in low-stage intercalation compounds.

The double-resonance Raman process, in GICs never studied before, has now been detected and explained as a proof of (almost) uncharged graphene layers present in the structure of potassium GICs [24]. Using the double resonance model introduced by Thomsen and Reich [120] one can describe the origin of D- and 2D-line modes as function of laser energy, as well as the splitting of the double resonance mode for double, triple, and multi-layer graphene [121, 122]. By considering the previous model and the existence of pristine uncharged graphene layers in stages III to VI, one conclude that the 2D-line in low-stages of GICs stems from these uncharged layers, because when just charged layers coexist (i.e. KC_{24}), no 2D-line is observed [24] (see Fig. 13 a). The number of interior graphene layers corresponds to the stage index n-2, i.e., stage III contains a mono-layer of uncharged graphene, stage IV a bi-layer graphene, stage V a tri-layer, and stage VI a quadri-layer graphene.

In order to proof the previous assumptions [24], the positions and splittings of the 2D-line for stages III to VI are extracted in Fig. 14 and the full electronic band-structure (DFT-LDA) for stage III KC_{36} (in ABA-stacking configuration) was calculated in Fig. 15 (black-line) and compared to the band-structure of charged pristine graphene (red and green). The unit-cell contains 24 atoms per carbon layer. Thus, the band-structure of pristine graphene (containing 2 atoms in the primitive unit cell) is plotted in a $2\sqrt{3}$x$2\sqrt{3}$ supercell. The high-symmetry point K of the Brillouin zone of graphene thus folds back onto Γ in the unit cell of KC_{36}. The red lines belong to the electronic bands of charged graphene with a Dirac point shifted down to ΔE_1 = 1.07 eV below the Fermi level which corresponds to a strong charging level, whereas green-lines depict the electronic states of weakly charged layers with a Dirac point shifted down by just ΔE_2 = 0.49 eV [24]. The band-structure plot demonstrates that

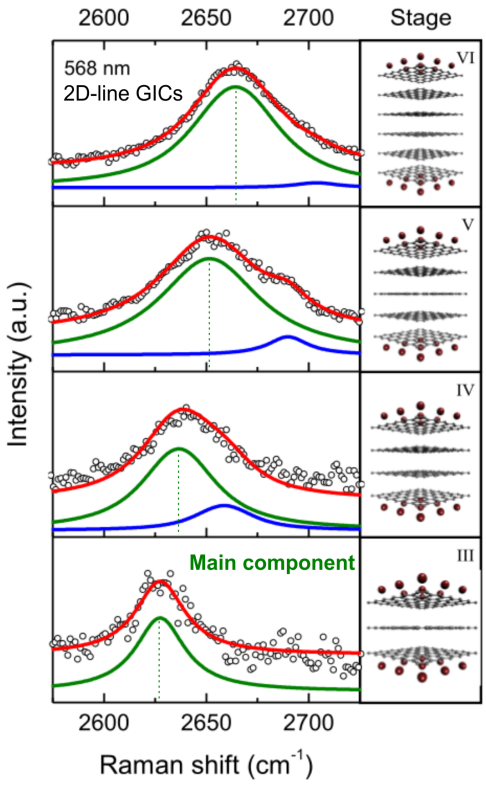

Figure 14 Detailed line-shape analysis of the 2D-line in stages III–VI adapted from Ref. [24] fitted with two Voigtian (green and blue lines). The result of the analysis is shown as a red line, while their corresponding approximate molecular structure are depicted on the right panel. The main component green is used to represent the strain effect form the interior layers in GICs.

the bands of the outer and inner layers in GICs are almost completely de-coupled, i.e., the band-structure of the GIC is mostly a superposition of the (shifted) band-structures of inner and outer graphene layers. Only at K (back-folded to Γ), the π-bands of the inner and outer layers couple through a lifting of the degeneracy at the Dirac-point and an avoided crossing of the charged (red) π^* band with the uncharged (green) π band.

Considering the possible vertical electron-hole pair transitions at 2.3 eV which may allow or block the double resonance process in graphene, one would expect equal phonon transitions with the same wave-vector **q** excited from KC_{36} and graphene, as their π-bands almost match exactly each other as seen on Fig. 15. Thus, three main effects come into place: i) The vertical transition (red) from a highly charged graphene layer gets barely above the Fermi level strongly suppressing the 2D-line transition and therefore confirming the absence of the 2D-line mode in KC_{24} and obviously in KC_8 too. ii) A vertical transition (green) from the uncharged graphene layers at the same energy crosses E_F and allows the double resonance process for graphene. The corresponding 2D-line is not shifted with respect to the one of pristine graphene, unless other effects come into play (see below). Finally iii) a vertical transition (blue) from the π-band of charged graphene to the π^*-band of the unchanged layers in KC_{36} is possible in principle. This would explain the red-shift of the 2D line, since a phonon closer to the Kohn-anomaly [123] in the highest optical branch around K would be excited. However, due to the spatial separation of charged and uncharged layers, the dipole-matrix element for this transition is almost zero and this this effect can be discarded. The question then arises what the origin of the strong down-shift of the 2D-line in KC_{36} is. Possibly, the environment of the uncharged layers, leads to a modification in the strong Kohn anomaly of the highest optical branch at K. These effects include a possible reduction of the electron-phonon coupling due to the (residual) charging [124], or a partial suppression of the Kohn anomaly due to hybridization with the outer layers (similar to the case when graphene gets closer to a Ni(111) surface [125]), or attenuation of the Kohn-anomaly via dielectric [126] screening or metallic screening [127, 128]. However, all of these mechanisms would lead rather to an up-shift of the 2D-line and not a strong down-shift. In Ref. [24] the noticeable down-shift was shown to stem from a lattice expansion (strain) of the graphene layers in GICs that head been measured in the early days of GIC research by Nixon and Parry [26] (see Fig. 5).[2] One can extract the frequencies of the phonon modes of the G and 2D lines of the uncharged layers in GICs by using the Grüneisen parameter

$$\gamma = -\frac{1}{\omega_0}\frac{\partial\omega}{\partial\varepsilon} \qquad (6)$$

and the induced strain from the experimental data. In Eq. 6, ω_0 is the Raman frequency of pristine graphene, $\partial\omega$ is the change in frequency due to induced strain $\partial\varepsilon$ (Bi-axial strain from Table 1), and γ = 2.2 and 3.3

[2] We have verified this lattice expansion by DFT-LDA calculations for the case of KC_{36}. While the experiments demonstrate a lattice expansion by 0.2% with respect to graphite (Table2), ab-initio calculations (full geometry-optimization of KC_{36} compared to fully relaxed graphite) yield a lattice expansion by 0.22%. This is in reasonable agreement with the experiment, given the intrinsic uncertainties of DFT in the determination of lattice constants. It is instructive to compare the lattice expansion of GICs to the lattice constant of pure doped graphene: if we put a charge density of $0.3310^{13}/cm^2$ (the calculated charge transfer from K to the outer layers in KC_{36}, see Table2), compensated by a homogeneous positive charge background in order to render the unit-cell neutral, we obtain a lattice expansion by 0.12% with respect to the lattice constant of graphite. This value is considerably smaller than the value for KC_{36}. This indicates that, for the lattice expansion, the location of the transferred charge (between the outer layer and the intercalant layer) as well as the presence of the K^+ ions play an important role.

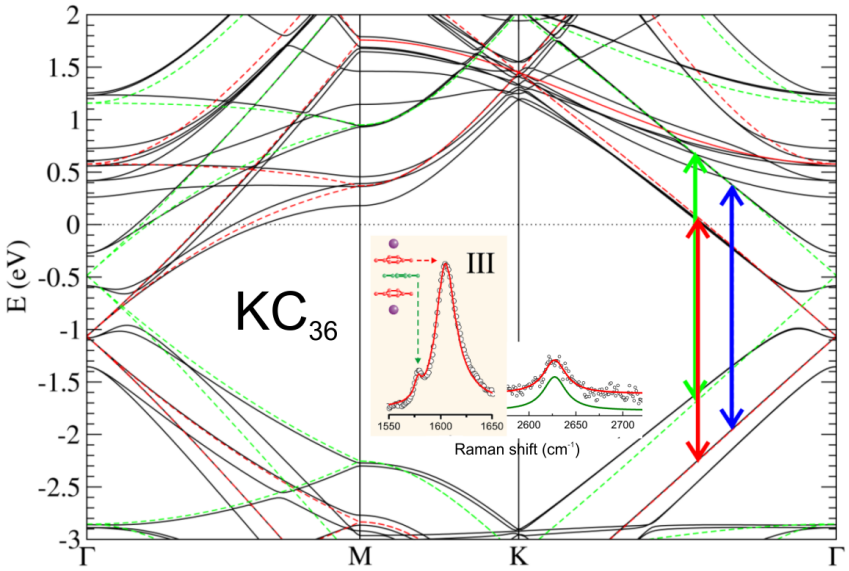

Figure 15 Band-structure of KC_{36} (black solid lines) vs. pristine graphene from *ab-initio* calculations adapted from Ref. [24]. The pristine graphene bands are shifted in energy to match the bands of the charged layer (red-dashed lines) and of the uncharged layer (green dashed lines). The red, green and blue vertical arrows mark the transition between the π-bands of the charged-charged, uncharged-uncharged and charged-uncharged layers at 2.3 eV laser energy.

respectively for the G- and 2D-line phonons [24, 129]. The resulting phonon-frequency shifts between pristine graphene and lattice-expanded graphene from Ref. [24] revealed that a down shift of the High Optical Branch (HOB) at K around 18 cm^{-1} occurs. This corresponds to a 2D-line redshift of 36 cm^{-1}. Thus, one can conclude that the down shift of the 2D-line observed in KC_{36} originates almost entirely from the small (but non-negligible) lattice expansion of the GIC. In contrast, the up-shift of the Gc-line originates mainly from the charge transferred from the potassium through the graphene boundary layers as will be summarized in the following section.

5 Strained and Charged Graphene Layers in GICs The recent study of the Raman response of highly stage GICs allowed to unambiguously disentangle charged, uncharged, and strained graphene layers within the structure of graphite intercalation compounds [24]. Although this has been already predicted by Pietronero and Strässler in 1981 [130] where they brought up the possibility to use the C-C bond distance in GICs as a tool to determine the charge transfer in these compounds, no detailed quantitative information regarding these effects was provided at that time allowing to separate those two effects. Now it is proven, that the Raman response of low-intercalation stages GICs is directly affected from: (i) the partial induced charge transferred from the K atoms into the carbon layers (Table 2), (ii) the in-plane bi-axial strain coming from the change in the C-C bond length (Table 2 and Fig. 5) and (iii) the relationship from these effects to the electronic band structures of the GICs (Fig. 15). Finally, considering all effects, the results are depicted in Fig. 16 from Ref. [24]. The following conclusions regarding the analysis of the Raman response of the G- and 2D-line in GICs and the implications for (multilayer) graphene have been derived:

G-line in GICs: It is experimentally described by two components which decrease in frequency according to the inverse stage n (see Fig. 16 a) (red circles)). This relates the frequency position of the G-line versus the inverse stage and its corresponding C-C bond length XRD studies [26]. By considering the well known G-line position of graphene [98, 121] (black dashed line in the figure), one can add the up-shift of the frequency coming from the transfer of charge density to graphene and subtract the down-shift from the bi-axial strain on graphene layers. Both contributions are depicted in this Fig. 16 a) as vertical green arrows (for the charge transfer related stiffening including the corresponding lattice expansion [119]) and vertical blue arrows (for the effective bi-axial strain). The results regarding the induced charge transfer to graphene are shown as green circles, while the effect of the induced strain looks like blue circles, and the difference from both are depicted as blue crosses.

The resulting Guc frequencies perfectly matched the experimental values. These results have been verified by *ab-initio* calculations by varying the lattice constant of pristine and charged graphene while the Grüneisen parameter remained constant for the charged values observed in GICs. The latter disclosed that both effects (charge transfer and strain) are truly additive, which means that around 50% of the change in frequency for the G_{uc} mode in GICs is related to charge transfer and the rest to induced strain.

The resulting Gc component in Fig. 16 a) has not yet been totally explained as its origin is more complex. The density charge observed to the boundary layers in GICs is shown to be above $4{\cdot}10^{13}/cm^{-2}$, which for instance must lead to a frequency value in the order of $\sim$1611 cm^{-1} in agreement to electronic gated graphene [45, 46], highly charged KC_{24} [39], and theoretically addressed by Lazzeri et al. [119]. Therefore, the calculated Gc values for each

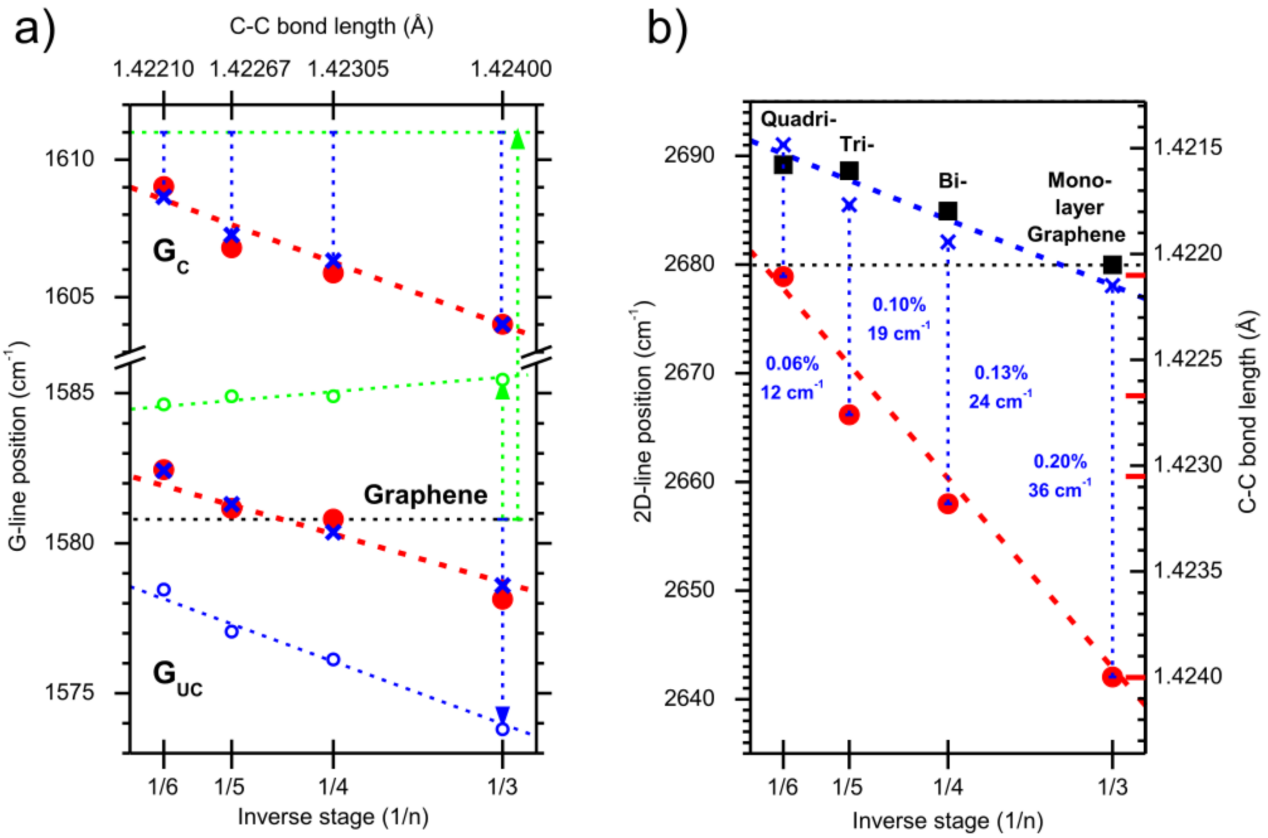

Figure 16 G- and 2D-line analysis in GICs with respect to strain and charge transfer from Ref. [24] a) the G-lines of the potassium GIC is depicted as function of the inverse stage. The upper x-scale depicts the C-C bond length of the XRD results of Ref. [26]. The dashed green lines and the green open circles show the G-line up-shift due to the high charge transfer to the charged G_c component and the remaining small charge transfer to the G_{uc} component. The blue dashed line and blue open circles come from the bi-axial strain induced softening of the G-line of graphene (black dashed line). The blue crosses depict the positions after adding the charge transfer and subtracting the internal strain. In panel b) the 2D-line position of the high-frequency-mode of GIC (red circles) and of unstrained (multi-layer) graphenes from Ref. [122] (black squares) is plotted as function of inverse stage. The dashed blue lines values in the figure depict the frequency softening by biaxial strain. The blue crosses depict the positions after subtracting this internal strain. The second y-scale depicts the C-C bond length owing a linear relation to the 2D line. The short red line are the experimental XRD bond length of the upper x-axes in panel a).

GIC considered an arbitrary value of charged transfer frequency of 1611 cm^{-1}, minus its corresponding effective bi-axial strain (the same as the one considered for the Guc) an almost perfect match of the resulting frequency is shown for the experimental G_c in Fig. 16 a).

The 2D-line in GICs, is observed only in higher staged GICs when $n \geq 3$. This is shown as red dots in Fig. 16 b) for the strongest component of the 2D-line shape analysis within the double resonance Model as depicted in Fig. 14. A linear decrease of the frequency was observed. This was compared to the experimental position of unstrained pristine mono-, bi-, tri-, and quadri-layer graphene from the literature (e.g. Ref. [122]) and depicted as black squares in the figure. In the case of the 2D-line, the up-shift resulting from the residual charge transfer of the uc layers was estimated to be less than 2 cm^{-1} [122] and could therefore be neglected in the analysis. On the other hand, the down-shift evaluated using the Grüneisen parameter for the 2D-line [129] lead to significant red shifts between 10 and 40 cm^{-1}. By artificially removing the biaxial strain the resulting values for the 2D-line in "unstrained "KC_{36}, KC_{48}, KC_{60}, and KC_{72} (blue crosses) could be compared to mono-, bi-, tri-, and quadri-layer graphene introduced above. A very good agreement has been shown in Fig. 16 b) which confirms that the 2D-line in GICs comes from the basically uncharged interior graphene layers. It also shows, that in this limit of a weak

charge transfer the position of the 2D response can be used as an accurate determination of the biaxial strain.

Going one step further in the analysis of these results, by comparing the 2D-line position to the absolute in-plane lattice constants of GICs [26] depicted as the right y-axes of Fig. 16 b), one can use it to determine the C-C bond distances for strained mono-, bi-, tri-, quadri-, and multi-layer graphene on an absolute scale. This allows to derive even in multi disperse polycrystalline samples or small individual graphene samples where XRD is not available. Therefore, the absolute lattice constant can be extracted by just measuring the 2D Raman frequency. The latter methodology brings an new alternative to XRD analyses with higher accuracy compared to the available one by electron diffraction experiments in electron microscopy. Furthermore, the method is contact free, simple and can be performed easily with reactive samples not suitable for ambient conditions.

6 Concluding remarks and open questions

In this feature article we have summarized how Raman spectroscopy gives some key contributions to the understanding of graphite intercalation compounds and have highlighted the developments from the early 80's until today. There were many open questions remaining from the first studies performed in this field and some of these questions are still open and calling for further experimental and theoretical study.

The Raman response of superconducting stage I GICs were revisited and their relation to defects and induced de-intercalation was reported as a crucial factor in the proper stage determination. The resonance Raman response of this stage was confirmed to be an asymmetric Fano-line at 1510 cm^{-1} with a c_z mode around 500 cm^{-1}. Stage II GICs were also reported as a stable intercalation phase after de-intercalating KC_8 with a single asymmetric line at 1610 cm^{-1} without double resonance Raman process. The detailed analysis of the EPC constant from the G-line response was compared with a full description of the underlying phonon density of states and the EPC using an analysis of the kink in the quasi-particle and structure in the ARPES response.

For highly staged GICs (stage III to VI) recent resonance Raman studies allow a direct stage identification from the intensity ratio R of the two G-line Raman components related to the heavily charged and weakly charged graphene layers. The low frequency mode of the G-line is attributed to the uncharged interior layers in GICs, whereas the high frequency is ascribed to the charged boundary layers. The vibrational frequency of both depends on the electron doping concentration and induced strain in the structure. A quantitative analysis of the charge transfer from *ab-initio* studies revealed that the charge transfer in GICs is incomplete. In addition, most (but not all) of the transferred charge brought from the potassium atoms remains on the charged graphene bounding layers adjacent to the intercalant. The effect of induced bi-axial strain in graphene has been linked to the C-C distance in GICs from early XRD analysis, revealing that this strain brings a homogeneous lattice parameter in the whole structure of the intercalation compound when $n \geq 3$. On the other hand, the analysis of the second order 2D-line Raman components in these GICs allows to unambiguously correlate the induced bi-axial strain to the graphene layers with the Raman frequency via the Grüneisen parameter.

From the application point of view Raman spectroscopy of GICs has therefore important implications in identifying and disentangling both internal strain and charge transfer in nanocarbon based materials. GICs may serve as a comparative bench mark for future nanoelectronic and optoelectronic devices as well as the local interfacial strain in graphene and carbon nanotube polymer composites on an absolute scale.

Acknowledgements We acknowledge financial support of the DRS Postdoc Fellowship Point-2014 of Freie Universität Berlin, and the FWF-I377-N16 project. L.W. acknowledges funding by the ANR (French National Research Agency) through project ANR-09-BLAN-0421-01. Calculations were done at the IDRIS supercomputing center, Orsay (Proj. No. 091827)

References

[1] M. J. Allen, V. C. Tung, and R. B. Kaner, Chem. Rev. **110**, 132–145 (2010).
[2] M. S. Dresselhaus and G. Dresselhaus, Adv. Phys. **30**(2), 139–326 (1981).
[3] W. Zhao, P. H. Tan, J. Liu, and A. C. Ferrari, J. Am. Chem. Soc. **133**, 5941–5946 (2011).
[4] K. E. Carr, Carbon **8**(2), 155–158 (1970).
[5] M. Inagaki, R. Tashiro, Y. Washino, and M. Toyoda, J. Phys. Chem. Solids **65**(2-3), 133–137 (2004).
[6] J. Lu, J. x. Yang, J. Wang, A. Lim, S. Wang, and K. P. Loh, ACS Nano **3**(8), 2367–2375 (2009).
[7] J. C. Chacon-Torres, Theory and Spectroscopy on functionalized Graphene and Graphite Intercalation Compounds, PhD thesis, University of Vienna, 2013.
[8] Y. Hernandez, V. Nicolosi, M. Lotya, F. M. Blighe, Z. Sun, S. De, I. T. McGovern, B. Holland, M. Byrne, Y. K. Gun'ko, J. J. Boland, P. Niraj, G. Duesberg, S. Krishnamurthy, R. Goodhue, J. Hutchison, V. Scardaci, A. C. Ferrari, and J. N. Coleman, Nat. Nanotechnol. **3**, 563–568 (2008).
[9] M. S. Dresselhaus and G. Dresselhaus, Adv. Phys. **51**, 1–186 (2002).
[10] G. L. Doll, M. H. Yang, and P. C. Eklund, Phys. Rev. B **35**, 9790–9798 (1987).
[11] M. H. Yang and P. C. Eklund, Phys. Rev. B **38**, 3505–3516 (1988).
[12] C. A. Howard, M. P. M. Dean, and F. Withers, Phys. Rev. B **84**, 241404 (2011).
[13] N. Emery, C. Herold, M. d'Astuto, V. Garcia, C. Bellin, J. F. Mareche, P. Lagrange, and G. Loupias, Phys. Rev. Lett. **95**, 087003 (2005).
[14] T. E. Weller, M. Ellerby, S. S. Saxena, R. P. Smith, and N. T. Skipper, Nat. Phys. **1**, 39–41 (2005).

[15] A. M. Dimiev, G. Ceriotti, N. Behabtu, D. Zakhidov, M. Pasquali, R. Saito, and J. M. Tour, ACS Nano **7**, 2773–2780 (2013).
[16] R. Nishitani, K. Ruda, and H. Suematsu, J. Phys. Soc. Jpn. **55**(5), 1601–1612 (1986).
[17] S. A. Solin and N. Caswell, J. Raman Spectrosc. **10**, 129–135 (1981).
[18] G. R. Hennig, Interstitial compounds of graphite, in: Progress in Inorganic Chemistry, (John Wiley & Sons, Inc., 2007), pp. 125–205.
[19] L. B. Ebert, Annu. Rev. Mater. Sci. **6**, 181–211 (1976).
[20] E. Stumpp, Mater. Sci. Eng. **31**, 53–59 (1977).
[21] R. J. Nemanich, S. A. Solin, and D. Guerard, Phys. Rev. B **16**, 2665–2672 (1977).
[22] S. A. Solin, The Nature and Structural Properties of Graphite Intercalation Compounds (John Wiley & Sons, Inc., 1982).
[23] N. Daumas and A. Herold, C. R. Seances Acad. Sci., Ser. C **268**, 373–375 (1969).
[24] J. C. Chacon-Torres, L. Wirtz, and T. Pichler, ACS Nano **7**(10), 9249–9259 (2013).
[25] S. A. Solin, Physica 99B p. 443 (1980).
[26] D. E. Nixon and G. S. Parry, J. Phys. C: Solid State Phys. **2**, 1732–1741 (1969).
[27] J. O. Besenhard and G. Eichinger, Journal of Electroanalytical Chemistry **68**(1), 1–18 (1976).
[28] G. Eichinger and J. O. Besenhard, Journal of Electroanalytical Chemistry **72**(1), 1–31 (1976).
[29] Z. Syrgiannis, B. Gebhardt, C. Dotzet, F. Hauke, R. Graupner, and A. Hirsch, Angewandte Chemie-international Edition **49**(19), 3322–3325 (2010).
[30] F. Liang, A. K. Sadana, A. Peera, J. Chattopadhyay, Z. N. Gu, R. H. Hauge, and W. E. Billups, Nano Letters **4**(7), 1257–1260 (2004).
[31] J. J. Stephenson, A. K. Sadana, A. L. Higginbotham, and J. M. Tour, Chemistry of Materials **18**(19), 4658–4661 (2006).
[32] J. M. Englert, C. Dotzer, G. Yang, M. Schmid, C. Papp, J. M. Gottfried, H. P. Steinrueck, E. Spiecker, F. Hauke, and A. Hirsch, Nature Chemistry **3**(4), 279–286 (2011).
[33] A. Hirsch, J. M. Englert, and F. Hauke, Accounts of Chemical Research **46**(1), 87–96 (2013).
[34] J. E. Fischer and T. E. Thompson, Phys. Today **31**, 36–& (1978).
[35] J. M. Zhang and P. C. Eklund, J. Mater. Res. **2**, 858–63 (1987).
[36] J. J. Ritsko, Physical Review B **25**(10), 6452–6459 (1982).
[37] D. M. Hwang, M. Utlaut, M. S. Isaacson, and S. A. Solin, Physical Review Letters **43**(12), 882–886 (1979).
[38] X. Liu, T. Pichler, M. Knupfer, M. S. Golden, J. Fink, H. Kataura, Y. Achiba, K. Hirahara, and S. Iijima, Physical Review B **65**(4), 045419 (2002).
[39] R. Parret, M. Paillet, J. R. Huntzinger, D. Nakabayashi, T. Michel, A. Tiberj, J. L. Sauvajol, and A. A. Zahab, ACS Nano **7**, 165–173 (2013).
[40] J. C. Chacon-Torres and T. Pichler, Phys. Status Solidi B **248**, 2744 (2011).
[41] M. Kalbac, H. Farhat, J. Kong, P. Janda, L. Kavan, and M. S. Dresselhaus, Nano Letters **11**(5), 1957–1963 (2011).
[42] J. Zhu, R. Jhaveri, and J. C. S. Woo, Applied Physics Letters **96**(19), 193503 (2010).
[43] B. Gao, A. Kleinhammes, X. P. Tang, C. Bower, L. Fleming, Y. Wu, and O. Zhou, Chemical Physics Letters **307**(3-4), 153–157 (1999).
[44] P. G. Bruce, B. Scrosati, and J. M. Tarascon, Angewandte Chemie-international Edition **47**(16), 2930–2946 (2008).
[45] A. Das, S. Pisana, B. Chakraborty, S. Piscanec, S. K. Saha, U. V. Waghmare, K. S. Novoselov, H. R. Krishnamurthy, A. K. Geim, A. C. Ferrari, and A. K. Sood, Nat. Nanotechnol. **3**, 210–215 (2008).
[46] A. Das, B. Chakraborty, S. Piscanec, S. Pisana, A. K. Sood, and A. C. Ferrari, Phys. Rev. B **79**, 155417 (2009).
[47] M. Inagaki, J. Mater. Res. **4**, 1560–1568 (1989).
[48] M. Endo, C. Kim, K. Nishimura, T. Fujino, and K. Miyashita, Carbon **38**(2), 183–197 (2000).
[49] M. Endo, Y. A. Kim, T. Hayashi, K. Nishimura, T. Matusita, K. Miyashita, and M. S. Dresselhaus, Carbon **39**(9), 1287–1297 (2001).
[50] M. Endo, Graphite intercalation compounds and applications (Oxford University Press, 2003).
[51] G. Hennig and L. Meyer, Phys. Rev. **87**, 439–439 (1952).
[52] N. B. Hannay, T. H. Geballe, B. T. Matthias, K. Andres, P. Schmidt, and D. Macnair, Phys. Rev. Lett. **14**, 225 (1965).
[53] M. Kobayashi and I. Tsujikawa, J. Phys. Soc. Jpn. **46**, 1945–1946 (1979).
[54] Y. Koike, H. Suematsu, K. Higuchi, and S. Tanuma, Physica B&C **99**, 503–508 (1980).
[55] I. T. Belash, A. D. Bronnikov, O. V. Zharikov, and A. V. Palnichenko, Solid State Commun. **69**, 921–923 (1989).
[56] I. T. Belash, A. D. Bronnikov, O. V. Zharikov, and A. V. Palnichenko, Synthetic Metals **36**(3), 283–302 (1990).
[57] R. M. Fleming, A. P. Ramirez, M. J. Rosseinsky, D. W. Murphy, R. C. Haddon, S. M. Zahurak, and A. V. Makhija, Nature **352**, 787–788 (1991).
[58] A. F. Hebard, M. J. Rosseinsky, R. C. Haddon, D. W. Murphy, S. H. Glarum, T. T. M. Palstra, A. P. Ramirez, and A. R. Kortan, Nature **350**, 600–601 (1991).
[59] M. J. Rosseinsky, A. P. Ramirez, S. H. Glarum, D. W. Murphy, R. C. Haddon, A. F. Hebard, T. T. M. Palstra, A. R. Kortan, S. M. Zahurak, and A. V. Makhija, Phys. Rev. Lett. **66**, 2830–2832 (1991).
[60] A. Y. Ganin, Y. Takabayashi, Y. Z. Khimyak, S. Margadonna, A. Tamai, M. J. Rosseinsky, and K. Prassides, Nat. Mater. **7**, 367–371 (2008).
[61] J. Hlinka, I. Gregora, J. Pokorny, C. Herold, N. Emery, J. F. Mareche, and P. Lagrange, Phys. Rev. B **76**, 144512 (2007).
[62] J. S. Kim, R. K. Kremer, L. Boeri, and F. S. Razavi, Phys. Rev. Lett. **96**, 217002 (2006).
[63] D. G. Hinks, D. Rosenmann, H. Claus, M. S. Bailey, and J. D. Jorgensen, Phys. Rev. B **75**, 014509 (2007).
[64] M. Calandra and F. Mauri, Phys. Rev. Lett. **95**, 237002 (2005).
[65] I. I. Mazin, L. Boeri, O. V. Dolgov, A. A. Golubov, G. B. Bachelet, M. Giantomassi, and O. K. Andersen, Phys. C **460**, 116–120 (2007).
[66] D. Allender, J. Bray, and J. Bardeen, Phys. Rev. B **7**, 1020–1029 (1973).

[67] G. Csanyi, P. B. Littlewood, A. H. Nevidomskyy, C. J. Pickard, and B. D. Simons, Nat. Phys. **1**, 42–45 (2005).
[68] I. I. Mazin, Phys. Rev. Lett. **95**, 227001 (2005).
[69] A. M. Saitta, M. Lazzeri, M. Calandra, and F. Mauri, Phys. Rev. Lett. **100**, 226401 (2008).
[70] J. C. Chacon-Torres, A. Y. Ganin, M. J. Rosseinsky, and T. Pichler, Phys. Rev. B **86**, 075406 (2012).
[71] M. Calandra and F. Mauri, Phys. Status Solidi B **243**, 3458–3463 (2006).
[72] M. P. M. Dean, C. A. Howard, S. S. Saxena, and M. Ellerby, Phys. Rev. B **81**, 045405 (2010).
[73] M. P. M. Dean, A. C. Walters, C. A. Howard, T. E. Weller, M. Calandra, F. Mauri, M. Ellerby, S. S. Saxena, A. Ivanov, and D. F. McMorrow, Physical Review B **82**(1), 014533 (2010).
[74] J. L. Sauvajol, N. Bendiab, E. Anglaret, and P. Petit, Comptes Rendus Physique **4**(9), 1035–1045 (2003).
[75] M. Paillet, P. Poncharal, A. Zahab, J. L. Sauvajol, J. C. Meyer, and S. Roth, Physical Review Letters **94**(23), 237401 (2005).
[76] P. C. Eklund and K. R. Subbaswamy, Phys. Rev. B **20**, 5157–5161 (1979).
[77] Y. Wang, P. Puech, I. Gerber, and A. Penicaud, Journal of Raman Spectroscopy **45**(3), 219–223 (2014).
[78] M. S. Dresselhaus, G. Dresselhaus, P. C. Eklund, and D. D. L. Chung, Mater. Sci. Eng. **31**, 141–152 (1977).
[79] A. Mialitsin, J. S. Kim, R. K. Kremer, and G. Blumberg, Phys. Rev. B **79**, 064503 (2009).
[80] G. L. Doll, P. C. Eklund, and J. E. Fischer, Phys. Rev. B **36**, 4940–4945 (1987).
[81] D. Guerard and A. Herold, Carbon **13**, 337–345 (1975).
[82] A. Grüeneis, C. Attaccalite, A. Rubio, D. V. Vyalikh, S. L. Molodtsov, J. Fink, R. Follath, W. Eberhardt, B. Buechner, and T. Pichler, Phys. Rev. B **79**, 205106 (2009).
[83] G. Profeta, M. Calandra, and F. Mauri, Nat. Phys. pp. 1–4 (2012).
[84] M. Calandra, G. Profeta, and F. Mauri, Physica Status Solidi B-basic Solid State Physics **249**(12), 2544–2548 (2012).
[85] A. Grüeneis, C. Attaccalite, A. Rubio, D. V. Vyalikh, S. L. Molodtsov, J. Fink, R. Follath, W. Eberhardt, B. Buechner, and T. Pichler, Phys. Rev. B **80**, 075431 (2009).
[86] L. M. Viculis, J. J. Mack, and R. B. Kaner, Science **299**, 1361–1361 (2003).
[87] L. M. Viculis, J. J. Mack, O. M. Mayer, H. T. Hahn, and R. B. Kaner, J. Mater. Chem. **15**, 974–978 (2005).
[88] A. K. Geim and K. S. Novoselov, Nat. Mater. **6**, 183–191 (2007).
[89] K. S. Novoselov, A. K. Geim, S. V. Morozov, D. Jiang, Y. Zhang, S. V. Dubonos, I. V. Grigorieva, and A. A. Firsov, Science **306**, 666–669 (2004).
[90] Y. B. Zhang, Y. W. Tan, H. L. Stormer, and P. Kim, Nature **438**, 201–204 (2005).
[91] A. A. Balandin, S. Ghosh, W. Bao, I. Calizo, D. Teweldebrhan, F. Miao, and C. N. Lau, Nano Lett. **8**, 902–907 (2008).
[92] I. W. Frank, D. M. Tanenbaum, A. M. Van der Zande, and P. L. McEuen, J. Vac. Sci. Technol., B **25**, 2558–2561 (2007).
[93] K. S. Novoselov, V. I. Falko, L. Colombo, P. R. Gellert, M. G. Schwab, and K. Kim, Nature **490**, 192–200 (2012).
[94] T. Ohta, A. Bostwick, T. Seyller, K. Horn, and E. Rotenberg, Science **313**, 951–954 (2006).
[95] S. Y. Zhou, G. H. Gweon, J. Graf, A. V. Fedorov, C. D. Spataru, R. D. Diehl, Y. Kopelevich, D. H. Lee, S. G. Louie, and A. Lanzara, Nat. Phys. **2**, 595–599 (2006).
[96] K. Sugawara, T. Sato, S. Souma, T. Takahashi, and H. Suematsu, Phys. Rev. Lett. **98**, 036801 (2007).
[97] A. Grüeneis, C. Attaccalite, T. Pichler, V. Zabolotnyy, H. Shiozawa, S. L. Molodtsov, D. Inosov, A. Koitzsch, M. Knupfer, J. Schiessling, R. Follath, R. Weber, P. Rudolf, L. Wirtz, and A. Rubio, Phys. Rev. Lett. **100**, 037601 (2008).
[98] Y. Y. Wang, Z. H. Ni, T. Yu, Z. X. Shen, H. M. Wang, Y. H. Wu, W. Chen, and A. T. S. Wee, J. Phys. Chem. C **112**, 10637–10640 (2008).
[99] A. Grüeneis and D. V. Vyalikh, Phys. Rev. B **77**, 193401 (2008).
[100] S. Kim, J. Ihm, H. J. Choi, and Y. W. Son, Phys. Rev. Lett. **100**, 176802 (2008).
[101] A. V. Fedorov, N. I. Verbitskiy, D. Haberer, C. Struzzi, L. Petaccia, D. Usachov, O. Y. Vilkov, D. V. Vyalikh, J. Fink, M. Knupfer, B. Buchner, and A. Gruneis, Nature Communications **5**(February), 3257 (2014).
[102] L. Boeri, G. B. Bachelet, M. Giantomassi, and O. K. Andersen, Physical Review B **76**(6), 064510 (2007).
[103] I. I. Mazin and A. V. Balatsky, Philosophical Magazine Letters **90**(10), 731–738 (2010).
[104] R. C. Haddon, A. F. Hebard, M. J. Rosseinsky, D. W. Murphy, S. J. Duclos, K. B. Lyons, B. Miller, J. M. Rosamilia, R. M. Fleming, A. R. Kortan, S. H. Glarum, A. V. Makhija, A. J. Muller, R. H. Eick, S. M. Zahurak, R. Tycko, G. Dabbagh, and F. A. Thiel, Nature **350**(6316), 320–322 (1991).
[105] O. Gunnarsson, Rev. Mod. Phys. **69**, 575–606 (1997).
[106] H. Kuzmany, M. Matus, B. Burger, and J. Winter, Advanced Materials **6**(10), 731–745 (1994).
[107] T. Pichler, A. Kukovecz, H. Kuzmany, H. Kataura, and Y. Achiba, Physical Review B **67**(12), 125416 (2003).
[108] T. Pichler, H. Kuzmany, H. Kataura, and Y. Achiba, Physical Review Letters **87**(26), 267401 (2001).
[109] J. Winter, H. Kuzmany, A. Soldatov, P. A. Persson, P. Jacobsson, and B. Sundqvist, Physical Review B **54**(24), 17486–17492 (1996).
[110] T. Pichler, New Diamond and Frontier Carbon Technology **11**(6), 375–397 (2001).
[111] S. Piscanec, M. Lazzeri, J. Robertson, A. C. Ferrari, and F. Mauri, Physical Review B **75**(3), 035427 (2007).
[112] N. Murata, J. Haruyama, J. Reppert, A. M. Rao, T. Koretsune, S. Saito, M. Matsudaira, and Y. Yagi, Physical Review Letters **101**(2), 027002 (2008).
[113] Z. K. Tang, L. Y. Zhang, N. Wang, X. X. Zhang, J. N. Wang, G. D. Li, Z. M. Li, G. H. Wen, C. T. Chan, and P. Sheng, Synthetic Metals **133**(March), PII S0379–6779(02)00408–3 (2003).
[114] L. Pietronero, S. Strassler, H. R. Zeller, and M. J. Rice, Physical Review Letters **41**(11), 763–767 (1978).
[115] C. Hartwigsen, W. Witschel, and E. Spohr, Phys. Rev. B **55**, 4953–4959 (1997).

[116] F. Ancilotto and F. Toigo, Phys. Rev. B **47**, 13713–13721 (1993).
[117] P. Giannozzi, S. Baroni, N. Bonini, M. Calandra, R. Car, C. Cavazzoni, D. Ceresoli, G. L. Chiarotti, M. Cococcioni, I. Dabo, A. Dal Corso, S. de Gironcoli, S. Fabris, G. Fratesi, R. Gebauer, U. Gerstmann, C. Gougoussis, A. Kokalj, M. Lazzeri, L. Martin-Samos, N. Marzari, F. Mauri, R. Mazzarello, S. Paolini, A. Pasquarello, L. Paulatto, C. Sbraccia, S. Scandolo, G. Sclauzero, A. P. Seitsonen, A. Smogunov, P. Umari, and R. M. Wentzcovitch, J. Phys.: Condens. Matter **21**, 395502 (2009).
[118] S. Pisana, M. Lazzeri, C. Casiraghi, K. S. Novoselov, A. K. Geim, A. C. Ferrari, and F. Mauri, Nat. Mater. **6**, 198–201 (2007).
[119] M. Lazzeri and F. Mauri, Phys. Rev. Lett. **97**, 266407 (2006).
[120] C. Thomsen and S. Reich, Phys. Rev. Lett. **85**, 5214–5217 (2000).
[121] A. C. Ferrari, J. C. Meyer, V. Scardaci, C. Casiraghi, M. Lazzeri, F. Mauri, S. Piscanec, D. Jiang, K. S. Novoselov, S. Roth, and A. K. Geim, Phys. Rev. Lett. **97**, 187401 (2006).
[122] D. Graf, F. Molitor, K. Ensslin, C. Stampfer, A. Jungen, C. Hierold, and L. Wirtz, Nano Lett. **7**, 238–242 (2007).
[123] S. Piscanec, M. Lazzeri, F. Mauri, A. C. Ferrari, and J. Robertson, Phys. Rev. Lett. **93**, 185503 (2004).
[124] C. Attaccalite, L. Wirtz, M. Lazzeri, F. Mauri, and A. Rubio, Nano Lett. **10**, 1172–1176 (2010).
[125] A. Allard and L. Wirtz, Nano Lett. **10**, 4335–4340 (2010).
[126] F. Forster, A. Molina-Sanchez, S. Engels, A. Epping, K. Watanabe, T. Taniguchi, L. Wirtz, and C. Stampfer, Phys. Rev. B **88**, 085419 (2013).
[127] M. Endlich, A. Molina-Sánchez, L. Wirtz, and J. Kröeger, Phys. Rev. B **88**(20), 205403 (2013).
[128] M. Endlich, H. P. C. Miranda, A. Molina-Sánchez, L. Wirtz, and J. Kröger, Ann. Phys. pp. n/a–n/a (2014).
[129] C. Metzger, S. Remi, M. Liu, S. V. Kusminskiy, A. H. Castro Neto, A. K. Swan, and B. B. Goldberg, Nano Lett. **10**, 6–10 (2010).
[130] L. Pietronero and S. Strassler, Phys. Rev. Lett. **47**, 593–596 (1981).